Aalto University
School of Science
Engineering Physics

Jani Taskinen

Crossover from Bose-Einstein condensation to lasing in plasmonic nanoparticle lattices

Master's Thesis
Espoo, May 6, 2019

Supervisor: Professor Päivi Törmä, Aalto University
Advisor: Professor Tommi Hakala, University of Eastern Finland

Aalto University
School of Science
Engineering Physics

ABSTRACT OF
MASTER'S THESIS

Author:	Jani Taskinen		
Title:	Crossover from Bose-Einstein condensation to lasing in plasmonic nanoparticle lattices		
Date:	May 6, 2019	**Pages:**	60
Major:	Engineering Physics	**Code:**	SCI3056
Supervisor:	Professor Päivi Törmä		
Advisor:	Professor Tommi Hakala		

Plasmonic nanoparticle lattices have recently been shown to support both lasing and Bose-Einstein condensation in the near infrared region of light. The basis for both phenomena is provided by plasmonic modes called surface lattice resonances which are combinations of array diffractions and individual plasmonic resonances in the nanoparticles. Both phenomena are easily produced in the same system by changing the periodicity of the lattice.

In this thesis the crossover from Bose-Einstein condensation to lasing is investigated by scanning the lattice periodicity from the condensation region to the lasing region and by varying spatially the pumping scheme. Both phenomena require the use of a fluorescent dye layer around the particle array and the effects of this layer are investigated by varying its thickness. The results suggest that achieving the lasing case with any periodicity requires the optical pumping to occur partially on top of the array where the feedback from the surface lattice resonance modes is present. The condensation of the plasmonic excitations can, however, occur even with the pump outside the array.

Keywords:	plasmonics, Bose-Einstein condensation, lasing
Language:	English

Aalto-yliopisto
Perustieteiden korkeakoulu
Teknillinen fysiikka

DIPLOMITYÖN
TIIVISTELMÄ

Tekijä: Jani Taskinen

Työn nimi:
Siirtymä Bose-Einstein kondensaatista laserointiin plasmonisissa nanopartikkelihiloissa

Päiväys:	6.5.2019	**Sivumäärä:**	60
Pääaine:	Teknillinen fysiikka	**Koodi:**	SCI3056
Valvoja:	Professori Päivi Törmä		
Ohjaaja:	Professori Tommi Hakala		

Plasmonisten nanopartikkelihilojen on viime aikoina osoitettu tukevan sekä laserointia että Bose-Einstein kondensaatiota lähellä valon infrapunataajuuksia. Ilmiöiden perustana ovat pintahilamoodit, jotka ovat metallisten partikkeleiden plasmonisten resonanssien sekä hilan aiheuttaman diffraktion yhdistelmiä. Molemmat ilmiöt voidaan toteuttaa samanlaisilla 2D-hilarakenteilla ja ainoa vaadittava muutos rakenteeseen on hilan jaksollisuuden muuttaminen.

Tässä työssä tutkitaan jo aiemmin havaittua muutosta laseroinnista kondensaatioon muuttamalla sekä partikkelihilan jaksollisuutta että systeemin pumppugeometriaa. Lisäksi tutkitaan molemmissa prosesseissa tarvittavan fluoresoivan väliainekerroksen paksuuden vaikutusta hilassa esiintyviin tiloihin. Tulokset viittaavat siihen että laserointitapauksen saavuttamiseksi optisen pumppauksen täytyy tapahtua ainakin osittain plasmonisen hilan päällä, missä pintahilamoodit ovat läsnä. Plasmonisten kvasipartikkeleiden kondensaatio voidaan kuitenkin havaita, vaikka pumppaus tapahtuisi hilan ulkopuolella.

Asiasanat: Plasmoniikka, Bose-Einstein kondensaatio, laserointi

Kieli: Englanti

Acknowledgements

The work for this Master's thesis was carried out in the Quantum Dynamics research group of the COMP Centre of Excellence at Aalto University. In addition, part of the research was performed in facilities provided by Micronova Nanofabrication Centre, supported by Aalto University.

First and foremost I would like to express my gratitude to Prof. Päivi Törmä for giving me the opportunity to join the Quantum Dynamics research group three years ago and to work on multiple unique projects which have given me more life experience that all my university studies combined. Being part of this group has taught me valuable lessons about who I am and what I wish to become.

I would also like to thank Prof. Tommi Hakala for the down-to-earth guidance throughout the years; I now know what I should strive for as a scientist. Thank you to Mr. Aaro Väkeväinen for the continuous hands-on support and mentoring inside and outside the lab. Thank you to Mr. Antti Moilanen for providing me with the tools and the occasional laugh I needed to complete my work with sanity. Thank you to Dr. Konstantinos Daskalakis for showing me what perfection means in reality. Thank you to Ms. Rebecca Heilmann and Mr. Alessandro Cotrufo for encouraging me throughout this project. In addition I would like to acknowledge the rest of the Quantum Dynamics group and especially the experimentalists with whom I did not have the chance to work extensively: Dr. Akbar Syed, Dr. Heikki Rekola and Dr. Rui Guo.

Most importantly, I would like to credit my parents and my sister who have given me uncompromising support anywhere, anytime. Finally, my dear Kirsi, I thank you for keeping me and our home in one piece when I have gone through some of the lowest points in my life.

Espoo, May 6, 2019

Jani Taskinen

Contents

1 Introduction **6**

2 Plasmonic nanoparticle array **8**
2.1 Surface plasmon polaritons 8
2.2 Surface lattice resonance modes 11

3 Bose-Einstein condensation and lasing **14**
3.1 Lasing in a plasmonic lattice 14
3.2 Plasmonic Bose-Einstein condensation 16
3.3 Photonic BEC-lasing-crossover 20

4 Experimental methods **23**
4.1 Sample fabrication 23
4.2 White light transmission measurements 25
4.3 BEC and lasing measurements 26
4.4 Experimental setup 27
4.5 Fabry–Pérot interference 32

5 Results **34**
5.1 Transmission experiments 34
5.2 Lasing and condensation experiments 36
5.2.1 Thermalization of SLR excitations and BE-distribution 36
5.2.2 Varying molecule layer thickness 39
5.2.3 Pump geometry 41

6 Conclusions **53**

Chapter 1

Introduction

Bose-Einstein condensation (BEC) is a fundamental quantum phenomenon which can be observed in a system of elementary particles called bosons. Proposed first by Satyendra Nath Bose and Albert Einstein in the 1920s, it describes the behavior of bosons in systems with low temperature and high particle density where the wave functions of particles begin to overlap. The quantum interactions in the system cause a macroscopically large population of bosons to accumulate to the lowest energy state [1]. Although there are few direct applications of investigating such quantum phenomena, one of the most prominent topics related to BEC is superconductivity which is understood as condensation of Cooper pairs [2].

The number of different systems which have been shown to support BEC is increasing and some of the latest additions to the list of particle that display BEC formation include exciton-polaritons [3, 4], magnons [5] and cavity photons [6]. Quite recently, the family of BEC systems has been extended to the field of plasmonics which is the study of light-matter interaction in metals. A metallic nanoparticle array can be combined with emission from a fluorescent dye medium creating a plasmonic system enabling strong light-matter interaction and light confinement [7–9]. Under optical pumping such a system can be used to generate and thermalize a population of plasmonic excitations to a band edge of the lattice modes [10]. With minor adjustments the structure can also be used to support lasing [11], that is to say the emission of optically amplified light based on stimulated emission. The physical processes behind the two phenomena are related but different and in the case of non-equilibrium exciton-polariton and microcavity photon condensates there has been discussion on whether such systems should be regarded as lasers or condensates [12–14] and how a crossover between the two cases can arise [15–17].

The crossover between lasing and condensation has been an increasingly popular topic in photon systems which in many ways resemble the plasmonic system discussed in this thesis. A condensation of photons can be realized in an optical microcavity filled with fluorescent dye solution [6]. The cavity provides a trapping potential in the system and continuous scattering from the dye molecules induce photon thermalization to the lowest energy state. Although in essence the bosonic particles existing in such a system are different from those of the plasmonic BEC, the similarities in the thermalization process and in the strength of the light-matter interaction are apparent. A brief review of the discoveries made in photon systems regarding lasing and condensation suggests promising outcomes for the similar plasmonic system [16–18].

The main objective of this thesis is to investigate the crossover between lasing and BEC in a plasmonic nanoparticle lattice experimentally. Both cases are demonstrated by fabricating the designated nanoparticle arrays and reproducing the results from previous studies [10, 11]. It has already been shown that the key parameter concerning the system dynamics is the lattice periodicity which can easily be tuned in order to reach both cases. In this work, it is shown that the pump geometry also has a significant impact on the transition between lasing and BEC cases. In addition to the crossover, the optical modes provided by the dye-lattice assembly are also examined in order to construct a more thorough understanding of the plasmonic system.

The contents of this thesis have been divided into six chapters including the introduction. Chapter 2 describes the basic optical properties of periodic plasmonic structures as they provide the basis for the plasmonic system investigated in this work. Chapter 3 introduces both lasing and Bose-Einstein condensation at a general level and describes how they are supported in a plasmonic nanoparticle system. It also includes a brief review of recent work done in the field of photon condensates. Chapter 4 goes over the experimental requisites for an optical system used to generate and measure the quantum phenomena introduced in the precious chapters. The results of the experiments are presented in Chapter 5. Finally, the conclusions and remarks of the work are given in Chapter 6 which also includes a discussion of possible system improvements and future topics related to these quantum phenomena.

Chapter 2

Plasmonic nanoparticle array

Plasmonics is the study of light-matter interaction mediated by electromagnetic excitations at a dielectric-metal interface. This chapter discusses the plasmonic modes found both in bulk metals as well as in nanoscale metallic structures which form the basis for plasmonic lasing and Bose-Einstein condensation.

2.1 Surface plasmon polaritons

The structure of metals can be modelled at a decent level by considering the metallic ions and their outer electrons as separate parts. The heavy, positively charged ions stay relatively still and occupy most of the space in the structure. They are surrounded and bonded together by a negatively charged electron cloud formed from the valence electrons of each metal atom. The metallic bonds keeping the structure together arise from the electrostatic force between the particles and they are fairly strong, although the structure is easily deformed as the ions are free to slide past each other. The electron cloud in metals is sometimes referred to as plasma and in the presence of an external electromagnetic wave the electrons begin to oscillate along with the changing electric field. A quantum of electron density oscillation in plasma is referred to as a plasmon.

The idea of immobile metallic ions accompanied by a surrounding electron cloud was first introduced in the Drude model by Paul Drude in 1900. By considering how a changing electric field affects the motion of free electrons, the model can be used to show that the frequency ω_p of plasma oscillations in a metal structure becomes

$$\omega_p = \sqrt{\frac{\rho_e e^2}{\varepsilon_0 m_e}}, \tag{2.1}$$

where ρ_e is electron density, e is elementary charge, ε_0 is vacuum permittivity and m_e is the mass of an electron [19].

In addition to oscillations in bulk metal it is also possible to observe plasmons at the interface of a metal and a dielectric in the form of surface plasmon polaritons (SPP) [20]. In SPPs the propagating electromagnetic fields in both media are combined with the plasma oscillations at the metal surface. The fields are confined to the interface and dissipate exponentially into both media. These quasi-particles propagate along the metal surface until ohmic losses cause them to die out or they scatter from surface impurities.

A dispersion relation describes how the wavelength or wavenumber of a wave is related to its frequency. The dispersion relation of SPPs propagating along a metal surface can be derived by considering Maxwell's equations at the metal-dielectric interface of non-magnetic media and it is given by

$$k_{||} = \frac{\omega}{c}\left[\frac{\varepsilon_1 \varepsilon_2(\omega)}{\varepsilon_1 + \varepsilon_2(\omega)}\right]^{1/2}, \tag{2.2}$$

where $k_{||}$ is the wavenumber of the SPP along the metal surface, ε_1 is the real relative permittivity of the dielectric medium, ε_2 is the frequency-dependent relative permittivity of the metal and c is the speed of light in vacuum [20]. Equation (2.2) is notably different compared to the strictly linear dispersion of light in free space:

$$k = \frac{\omega}{c}. \tag{2.3}$$

Examples of dispersion relations of SPPs and light (Equations (2.2) and (2.3)) are shown in Figure 2.1 with red and blue solid lines, respectively. The metal surface is in vacuum ($\varepsilon_1 = 1$) and the metal relative permittivity is assumed to be the free electron expression $\varepsilon_2(\omega) = 1 - \omega_p^2/\omega^2$ [21]. The figure also shows the surface plasma oscillation frequency which is an asymptote of the SPP dispersion curve.

If an external electromagnetic field is coupled to an SPP, the resonant modes are called surface plasmon resonances (SPRs). Coupling SPPs to photons allows one to both excite and detect SPPs via light. There are two requirements for coupling SPPs with photons. First, the frequency of light must match that of the polariton which can easily be achieved by tuning the photon frequency. Second, the tangential component of the photon wave vector has to match the wavenumber of the SPP. This cannot be achieved in free

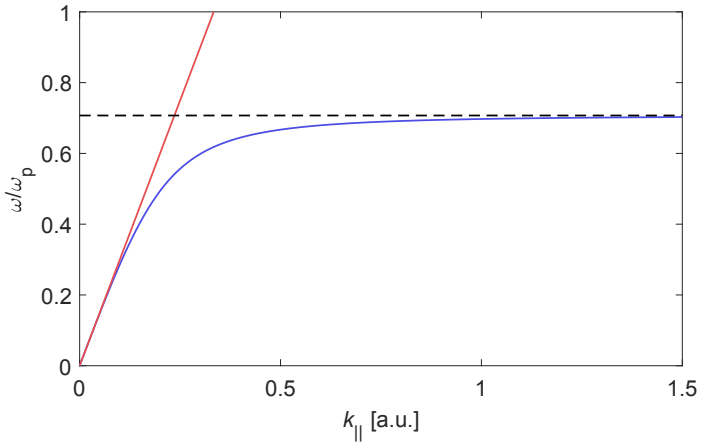

Figure 2.1: Dispersion relations of SPPs at a metal-vacuum interface (blue solid line) and light in free space (red line). The surface plasma frequency ($\omega_{sp} = \omega_p/\sqrt{2}$), which is an asymptote of the SPP dispersion, is marked with a black dashed line.

space as the dispersion of SPPs never crosses that of light in [20] (see Figure 2.1). An SPP always has more momentum compared to a photon of the same frequency. To overcome this, it is possible to utilize total internal reflection to increase the tangential wave vector of light. Otto and Kretschmann configurations [21] are two examples of setups which use a prism to match the momentum of photons and SPPs.

In addition to SPPs, it is possible to couple light with plasma oscillations that do not propagate by modifying the structure of the metal surface. These localized surface plasmon resonances (LSPRs) appear in metallic nanoparticles or voids of different geometries [22]. The electric field of the incident light causes the electrons in the nanoparticles to redistribute the electric charge. This induces the Coulomb attractions in the particles to work as a restoring force for the plasma oscillations. LSPRs are confined to the spatial dimensions of the nanoparticle and it is therefore evident that the shape and size of the particles affect the frequencies of the LSPRs, in addition to the dielectric constant of the metal and its surroundings. Excitation of LSPRs by incident light requires one to only match the frequency and polarization of light with the localized surface plasmon [23]. This leads to the enhancement of local electromagnetic fields in the particle, intense absorption bands and strong scattering of light [24]. The near-fields and scattering cross-sections of a small metallic particle can be calculated by solving the Helmholtz equation for the given object with the quasi-static approximation which leads to

a Laplace equation. The quasi-static approximation assumes that the size of the object is negligible compared to the wavelength of the electromagnetic radiation so that each part of the object experiences the same external field [22].

2.2 Surface lattice resonance modes

If metallic nanoparticles are arranged in a periodic ensemble so that the interparticle distance is similar to the wavelength of light in the surrounding medium, new collective modes called surface lattice resonance (SLR) modes appear. These modes are a combination of the LSPRs of the individual nanoparticles and the diffracted orders (DO) of the periodic lattice [25]. The mode energies, losses and density of states can be tuned by varying the lattice periodicity and nanoparticle geometry. SLRs exhibit extremely narrow linewidths which correspond to long mode lifetimes [7, 8, 26].

A simple way to describe the dispersion of the SLR modes in a two-dimensional periodic lattice is to consider how the periodicity of the lattice affects the dispersion of plane waves. In free space the dispersion relation between energy E and wavenumber components k_y and k_x is

$$k_x^2 + k_y^2 = \left(\frac{En}{\hbar c}\right)^2, \tag{2.4}$$

where n is the refractive index of the surrounding medium, $\hbar$ is the reduced Planck constant and $|\mathbf{k}| = \sqrt{k_x^2 + k_y^2}$ where only the two-dimensional case is considered so that $k_z = 0$ [25]. Equation (2.4) describes the dispersion of the scattered light from each particle in the array. The nanoparticles are assumed to be point-like dipoles driven by an x-polarized light and they are arranged in a periodic square array with periodicities p_x and p_y in the x and y-directions, respectively. The interparticle distance must be long enough to prevent near-field coupling and the generation of multipoles [25]. As the driving field is x-polarized, the particles radiate mostly in the y-direction.

The periodicity of the lattice causes the dispersion relation in Equation (2.4) to be copied to higher wavenumbers generating the diffracted orders of the lattice. Since the nanoparticles mostly radiate in the y-direction, the periodicity in the x-direction has no effect on the dispersion and it is enough to consider the y-periodicity. The momentum kicks G_y provided by the lattice are inversely proportional to the lattice periodicity:

$$G_y = \frac{2\pi}{p_y}. \tag{2.5}$$

In momentum space the spacing between each diffracted order is a multiple of a single momentum kick. The first diffracted orders (0,+1) and (0,-1) cross at $k_y = k_x = 0$ which is also referred to as the Γ-point. The energy at the crossing of the first diffracted orders is

$$E_\Gamma = \frac{hc}{np_y}, \tag{2.6}$$

where h is the Planck constant. The light cones described by Equation (2.4) are plotted in Figure 2.2 for the first two diffracted orders.

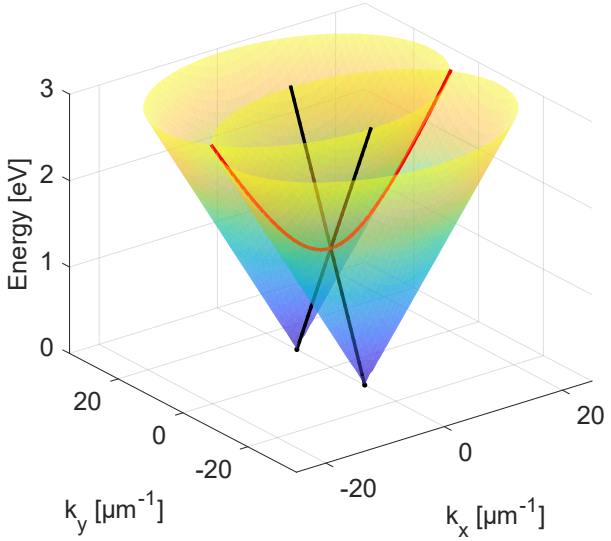

Figure 2.2: Light cones of the (0,+1) and (0,-1) diffracted orders in momentum space. The TM and TE modes are shown as red and black solid lines, respectively. The refractive index is 1.5.

By considering either the $k_y = 0$ or the $k_x = 0$ plane, two different modes can be observed: transverse electric (TE) at $k_x = 0$ and transverse magnetic (TM) at $k_y = 0$. The TE modes display a linear dispersion from the (0,+1) and (0,-1) diffracted orders which cross at the Γ-point. The dispersion relation of this mode is

$$E = \frac{\hbar c}{n}(\pm k_y + G_y). \tag{2.7}$$

The TM mode on the other hand has a square root dependence as the momentum G_y given by the lattice is perpendicular to the incident light. The dispersion relation of the TM-mode is

$$E = \frac{\hbar c}{n}(k_x^2 + G_y^2)^{1/2}. \tag{2.8}$$

Near the Γ-point ($k_x \ll G_y$) the TM-mode is approximately quadratic [25]. Energy at the Γ-point is the same in both modes.

At the crossing of the (0,+1) and (0,-1) diffracted orders, there are two modes degenerate in energy. Scattering from the nanoparticles provides a coupling between the two counterpropagating modes which results in two hybrid modes: symmetric and antisymmetric [25]. In addition, a small photonic band gap is formed between the upper and lower dispersion branches. The band gap originates from the periodic structure of the lattice which causes a periodic change in the refractive index along the plane of the array. At the Γ-point the electromagnetic field in the lattice is a standing wave field. There are two symmetric locations where the node of the electric field can exist [27]. First option is directly on the nanoparticle which generates quadrupole excitations which cannot be observed in the far-field. This mode is also called a dark mode and it can only be detected indirectly, for instance, via effects caused by the finite size of the lattice [11]. The other option for the location of the electric field node is between two nanoparticles which induces dipoles in the nanoparticles. This mode is called a bright mode as the far-field radiation of the dipoles is detectable. The waves in the two modes experience a different environment due to the periodic refractive index and an energy difference between the modes can be observed as a band gap in the lattice dispersion. The chosen geometry of the nanoparticles determines which mode appears in the upper SLR branch and which mode in the lower branch [25]. Here, rod-shaped particles are used as they allow the bright mode to exist in the upper SLR branch creating a continuous band edge where the plasmonic BEC can be formed.

A more comprehensive calculation of the lattice modes can be obtained using the coupled dipole approximation [28] where each nanoparticle is represented as a discrete dipole whose polarizability is dependent on the material and geometry of the particle. The dipole moment at each particle is affected by the driving field and the field from other dipoles, so that a set of linear equations can be constructed. The field at each nanoparticle and the extinction cross of the system can then be solved from the equations [7].

Chapter 3

Bose-Einstein condensation and lasing

Combining the plasmonic structures presented in the previous chapter with fluorescent dyes creates new and exciting platforms for investigating light-matter interactions in ultrafast timescales and small mode volumes. Emission from dye molecules couples to plasmonic modes in the vicinity of metallic nanoparticles and can therefore be modified by tailoring the mode characteristics.

In this chapter, different phenomena relying on light-matter interactions in both plasmonics and optics are described. First, the principle of lasing in a plasmonic nanoparticle lattice is introduced. Second, the recently discovered BEC in an almost identical system is discussed along with a small review of photonic systems that support condensation. Photon condensates are of great interest as they share some similarities with the plasmonic BEC and they have already shown promising steps in describing the crossover between lasing and BEC.

3.1 Lasing in a plasmonic lattice

Laser is a device which uses the process of stimulated emission to emit spatially and temporally coherent light [29]. Temporal coherence tells us how well a wave can interfere with itself at different times. Spatial coherence on the other hand measures the correlation between two points in space. Producing coherent light in a plasmonic lattice has already been demonstrated and one of the major advantages of a system is the easily tunable nanoscale structure [11].

In plasmonic lasing the SLR modes described in section 2.2 are coupled with emission from fluorescent molecules. Emission is the process of a quantum mechanical state transitioning to a lower energy state resulting in the emission of a photon. The energy of the emitted photon is equal to the energy difference between the states. Emission is the inverse process of absorption where the energy of a photon is taken up by matter causing particles to transition from low energy states to higher energy states.

Emission from chemical elements or compounds can occur either spontaneously or via stimulated emission. In spontaneous emission the transition from the higher state to the lower state occurs without an external field. The mechanism behind spontaneous emission comes from vacuum field fluctuations; in quantum electrodynamics the fields have non-zero energy even in the ground state just like a harmonic oscillator has a ground state energy of $\hbar\omega/2 \neq 0$. These vacuum fluctuations allow the excited energy state to couple to the electromagnetic field and set off the spontaneous emission process [30]. The direction, phase and polarization of the emitted photon are random in this case.

Stimulated emission on the other hand occurs in the presence of an external electromagnetic field. When an incident photon of a suitable frequency meets an excited atom or molecule, coupling between the excited state and the field causes the particle to emit a photon whose energy, phase, polarization and direction are identical to the original photon.

Stimulated emission provides the mechanism for optical amplification in laser systems. The signal from a single photon can be amplified multiple times by guiding it through a gain medium of excited particles. If the energy of the photon matches a transition between the energy states of the particles, the photon can be either absorbed in the ground state particles or it can stimulate a photon to be emitted by the excited particles. An external energy source can be used to excite more than 50% of the particle population in the gain medium. This situation is also referred to as population inversion. In this case a photon propagating through the gain medium causes a chain reaction of stimulated photon emissions and the original signal of the incident photon is multiplied. In conventional laser systems the gain medium is usually placed in an optical cavity between two reflecting mirrors. The emitted photons propagate through the gain medium multiple times by reflecting back and forth from the cavity mirrors and form a beam of coherent laser light. The feedback provided by the cavity is crucial in the process as only the resonant cavity modes experience constructive interference and can be amplified.

The lasing process in a plasmonic nanoparticle lattice is similar to the conventional lasing in an optical cavity although the system has no phys-

ical cavity mirrors. The gain medium in the plasmonic system consists of fluorescent molecules dissolved in a transparent solvent. A thin layer of the molecule mixture is laid on top of the nanoparticle array either by spin-coating or sealing it under another glass slide. In order to reach population inversion the gain medium is pumped with an external fs-laser and the photons emitted from the molecules couple to the SLR modes of the lattice. The SLR modes provide the required feedback for the optical amplification in the system and, as a result, narrow emission peaks can be observed [11]. These peaks show nonlinear increase of emission and reduction of linewidth as well as blue shift in emission with increasing pump fluence, all of which are signatures of lasing.

3.2 Plasmonic Bose-Einstein condensation

Bose-Einstein condensation is a fundamental quantum phenomenon where quantum statistics of the bosons generate a macroscopic population in the ground state of a quantum mechanical system. Bosons are one of two species of elementary particles that exist. What differentiates bosons from the other particle type, fermions, is their behavior in systems where quantum statistics becomes significant and the particle wavefunctions begin to overlap. The characteristic signature of fermions is that there cannot exist two fermions in one quantum mechanical state. This is most apparent in atoms where electron orbitals can only hold two electrons with opposite spins. It is also known as the Pauli exclusion principle. Bosons, on the other hand, can occupy the same quantum state which is the basic requirement for a BEC to occur.

The fact that bosons are indistinguishable and capable of occupying the same state allows one to show how the famous Bose-Einstein distribution arises from statistical mechanics. Consider a system with occupied one-particle states i whose energies are denoted as E_i and degeneracies as g_i. The number of particles in state i is n_i so that the total number of particles in the system $N = \sum_i n_i$ and the total energy in the system $E = \sum_i E_i n_i$ are constant and limit the system. In state i the bosons may occupy the degenerate one-particle states in multiple different ways since they can also occupy the same state. Using combinatorics the number of different ways Q_i to arrange the bosons in state i becomes [30]

$$Q_i = \frac{(n_i + g_i - 1)!}{n_i!(g_i - 1)!} \tag{3.1}$$

and the total number of possible configurations Q over all states i becomes a product of these terms:

$$Q = \prod_i \frac{(n_i + g_i - 1)!}{n_i!(g_i - 1)!}. \tag{3.2}$$

The most probable configuration in thermal equilibrium is the one that can be achieved in the largest number of different ways which means that in order to find the distribution of bosons in such a system, Q must be maximized. It is also more convenient to maximize the logarithm of Q to shift from products to sums. Logarithm is a monotonic function so its maximum is also the maximum of its argument. Since the total energy and particle number has to be conserved the method of Lagrange multipliers is used. The logarithm of Q is combined with the energy and particle restriction to get a new function F:

$$\begin{aligned} F =& \ln(Q) + \beta_1\big(N - \sum_i n_i\big) + \beta_2\big(E - \sum_i E_i n_i\big) \\ =& \sum_i \{\ln[(n_i + g_i - 1)!] - \ln(n_i!) - \ln[(g_i - 1)!]\} \\ &+ \beta_1\big(N - \sum_i n_i\big) + \beta_2\big(E - \sum_i E_i n_i\big), \end{aligned} \tag{3.3}$$

where β_1 and β_2 are the Lagrange multipliers. Assuming that the occupation numbers are large, it is possible to use Stirling's approximation:

$$\ln(n_i!) \approx n_i \ln(n_i) - n_i, \quad x \gg 1. \tag{3.4}$$

Applying Stirling's formula to Equation (3.3) gives

$$\begin{aligned} F \approx& \sum_i \{(n_i + g_i - 1)\ln(n_i + g_i - 1) - (n_i + g_i - 1) + n_i \ln(n_i) \\ &- n_i - \ln[(g_i - 1)!]\} + \beta_1\big(N - \sum_i n_i\big) + \beta_2\big(E - \sum_i E_i n_i\big). \end{aligned} \tag{3.5}$$

The maximum of Q is found by setting the derivative of F with respect to n_i equal to zero which gives

$$\ln(n_i + g_i - 1) - \ln(n_i) - \beta_1 - \beta_2 E_i = 0. \tag{3.6}$$

Solving for n_i in Equation (3.6) gives the most probable occupation number for state i:

$$n_i = \frac{g_i}{e^{(\beta_1+\beta_2 E_i)} - 1}, \tag{3.7}$$

where the degeneracy of the state i was assumed to be large so that $g_i - 1 \approx g_i$. The physical interpretation of the Lagrange multipliers can be shown to be related to the temperature T and chemical potential μ in the system:

$$\begin{aligned} \beta_1 &= \frac{1}{k_B T} \\ \beta_2 &= -\frac{\mu}{k_B T}, \end{aligned} \tag{3.8}$$

where k_B is the Boltzmann constant [30]. Combining (3.8) with Equation (3.7) we arrive in the famous Bose-Einstein (BE) distribution:

$$n(E) = \frac{g(E)}{e^{(E-\mu)/k_B T} - 1}. \tag{3.9}$$

In a similar fashion, one is able to reproduce the Maxwell-Boltzmann (MB) distribution as

$$n(E) = \frac{g(E)}{e^{(E-\mu)/k_B T}}. \tag{3.10}$$

The MB-distribution describes the behavior of classical particle that are identical yet distinguishable from each other. Equations (3.9) and (3.10) are plotted in Figure 3.1. It is notable that in the high energy region the BE-distribution approaches the MB-distribution.

Chemical potential μ corresponds to the change in free energy of a system when a particle of the given species is added to the system [31]. In a system with bosons which follow the Bose-Einstein distribution given by Equation (3.9), the ground state with energy E_0 must have an occupation of $n(E_0) \geq 0$ for any T which means that $\mu \leq E_0$. At high temperatures, chemical potential in the system is much smaller than the ground state energy but as the temperature is lowered, chemical potential in the system increases until it reaches E_0. The maximum particle density in the excited states increases with μ and saturates when $\mu = E_0$ which can be seen from Equation 3.9. If the actual density of particles is greater than the maximum density, the extra particles must accumulate to the ground state whose occupation number can be arbitrarily large. A macroscopic population of particles occupies the ground state of the system and a Bose-Einstein condensation is formed.

The first experimental observations of BEC took place in 1995 [32, 33] in ultracold dilute atomic vapors but recently there has been a shift from

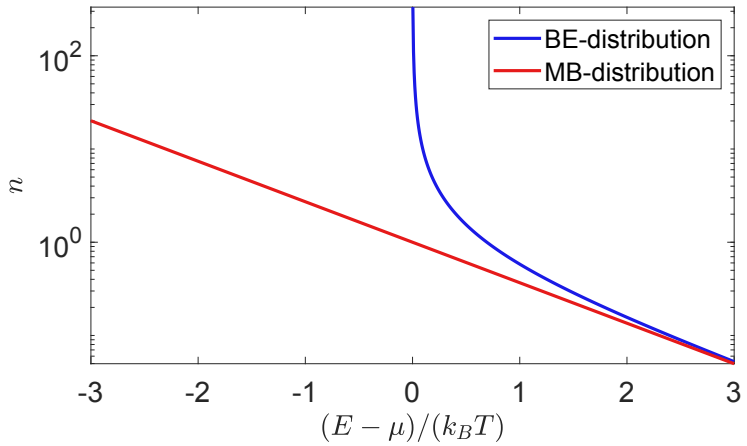

Figure 3.1: Bose-Einstein (blue line) and Maxwell–Boltzmann (red line) distributions. The BE-distribution diverges at $E = \mu$ and converges to the MB-distribution in the high energy limit.

these textbook atomic condensates to systems that can form a BEC even at room temperature. For instance, exciton-polaritons [3, 4] and microcavity photons [6] have been used to demonstrate condensation phenomena in high temperature conditions. The bosonic particles leak out of these non-equilibrium systems and the accumulation to the ground state is enabled by the short thermalization timescales. The distinction between equilibrium and non-equilibrium condensates is not exact as even the equilibrium of cold atomic BEC is not perfect: the gaseous vapor can escape the condensation trap and it is also gradually converted into a solid on a time scale of many seconds [34]. Only in liquid helium is the number of particles truly conserved.

As mentioned earlier, the nanoparticle system introduced in Section 2.2 has been shown to support the formation of a plasmonic BEC [10]. The system is similar to the plasmonic lasing case where the lattice is submerged in a fluorescent dye layer and the dye molecules are weakly coupled to the SLR modes. The molecules are excited via optical pumping in the high energy region and the spontaneously emitted photons induce SLR excitations in the lattice. The key difference to the lasing experiment is that the lattice itself does not experience pumping; the pump laser is used to excite only the molecules at the edge of the array. When the photon part of the SLR excitation is absorbed to a rovibrational level of the excited molecule state, it is likely to drop to one of the lower levels before being emitted again. As the SLR excitations propagate along the array, the continuous cycles of absorption and re-emission cause the energy of the SLR population to drop as the

dye layer provides a room temperature bath for the excitations. The cycles continue until the energy of the quasiparticle is so low that the molecules are no longer able to absorb them. This energy is called the absorption edge.

A critical point in the thermalization process occurs near the Γ-point. If the nanoparicles are rod-shaped, the upper branch will have a continuous band edge which functions as a ground state for the condensation process. If the absorption edge is matched with the dispersion, the thermalization process stops and the SLR population begins to accumulate. In this case the system forms a plasmonic BEC. If the absorption edge is below the band edge, it is possible for the excitations to be absorbed across the band gap and continue the thermalization process in the lower SLR branches. If the absorption edge is above the band edge, the absorption-emission cycles are suppressed near the band edge and the system behaves more like a laser without a thermalizating population [10]. Matching the SLR band edge to the absorption edge is easily accomplished by varying the lattice periodicity.

The transition from condensation to the lasing case has been achieved by gradually varying the lattice periodicity [10] but in this thesis the main goal is to investigate the crossover more thoroughly by also varying the location of the pump spot. Investigating the spatial effect of the pumping is critical for future research as the repeatability of the experiments is highly dependent on how well defined the system parameters are. Currently there is no precise norm for the spot location other than an approximate distance from the array edge. In addition, previous experiments with similar samples have displayed unknown modes close to the SLR band edge which greatly affects how well the plasmonic phenomena in the lattice can be observed. The possible origin of these modes is investigated by modifying the dye layer thickness. The experiments and array structures are described in more detail in Chapter 4.

3.3 Photonic BEC-lasing-crossover

The BEC of photons is closely related to the plasmonic BEC of SLR excitations as the thermalization processes are similar and both phenomena appear in the weak coupling regime of light-matter interaction. In both systems the bosonic particles (photons or SLR excitations) are brought to the ground state via continuous cycles of absorption and re-emission in a fluorescent medium [6, 10]. The system supporting photonic BEC has also been shown to switch to laser-like behavior under certain conditions. In addition to experiment, theoretical work has been done to describe the condensation process using a non-equilibrium model that predicts the possibility of a crossover between photon condensation and traditional laser behavior [16, 18].

One condition for reaching a textbook equilibrium BEC is the possibility of a system to reach thermal equilibrium. A simple way to reach equilibrium in a Bose gas of photons is the black-body radiation. A black-body is a theoretical object that absorbs all incident electromagnetic radiation regardless of frequency or incident angle. Radiation experiences no transmission or reflection as all energy is absorbed. Once a black body reaches thermal equilibrium with its surroundings, the electromagnetic radiation emitted from it is called black-body radiation whose spectrum follows Planck's radiation law [35]. The radiation is only dependent on the equilibrium temperature, not for instance on the shape of the black body. An example of a decent black body is a cavity made out of black walls. The photons emitted in such a system are in thermal equilibrium with the black body but as temperature goes down, they start to disappear into the walls instead of accumulating to the ground energy level. The photon number is not conserved and the chemical potential is either zero or not well defined depending on the point of view [36].

The lack of number-conserving thermalization processes has inspired some suggestions for a photon condensation method [37, 38] until in 2010 a BEC of photons was achieved in a dye-filled optical microcavity consisting of two curved mirrors enclosing a fluorescent medium [6]. The system acts as a white-wall box where more than 99.997% of incident light is reflected from the cavity walls which provide confinement and a non-vanishing photon mass. The two near-planar mirrors are placed a few wavelengths apart which modifies the free spectral range, the difference between two longitudal modes, to be as large as the spectral width of the dye. This constricts the possible longitudal modes in the cavity so that the emission of the chosen mode number dominates over other emission, and only the transverse modes allow emission at different energies. As a consequence, the photons in the microcavity can be treated as a two-dimensional photon gas. The curvature of the mirrors provides a harmonic trapping potential for the system and the dispersion relation near the center of the trap becomes quadratic. The mode without a transverse component becomes the ground state of the system with the lowest possible frequency, the cut-off frequency.

The thermalization process in photon condensation is similar to the one in the plasmonic system. Dye molecules inside the cavity are excited using high intensity laser pulses. The excited molecules emit photons which begin to collide with the dye solution which functions as a heat bath for the photons. The photons are absorbed and re-emitted continuously inside the cavity and during each cycle the excited energy states of the molecules thermalize and the energy of the photons is lowered until they reach the frequency cut-off.

With increased pumping the system shows a spectrally sharp peak at the lowest energy state accompanied by a broad thermal tail [6].

There is a small loss rate in the system due to the finite reflectivity of the cavity mirrors. In addition, the system experiences other losses due to coupling into unconfined optical modes and finite quantum efficiency [6]. The photons can reach equilibrium only if the thermalization timescale is short compared to the loss rate of the cavity walls. The loss rate and the absorption of the dye molecules at the lowest energy state are wavelength-dependent and can therefore be easily adjusted by varying the cut-off frequency via mirror geometry. The interplay of loss and thermalization rates modified by the cut-off frequency allows the system to switch between photon condensation and laser-like behavior. With a high cut-off frequency the cavity provides the photons with a short thermalization timescale and photon BEC can be achieved. With a low cut-off frequency the photons escape the cavity before they have time to reach the lowest energy state and the system resembles a mode-locked laser [16].

A theoretical model based on the steady state properties of the photon BEC system has also been developed in order to describe both the condensation of photons as well as the laser-like behavior [17, 18]. The model, which takes into account the pump and decay processes present in the photon BEC system, is able to predict the transition to a condensed phase and also how the equilibrium is dependent on pump power and temperature. The conclusion is the same as in the experimental work: the destruction of a thermalization process in the system is due to the interplay between gain and loss which can both be adjusted via the cut-off frequency. The model shows that by decreasing the temperature, increasing the losses or detuning the cut-off frequency from the molecule absorption, the system transitions into laser-like behavior [17]. This suggests that a smooth crossover from a condensation process to a laser is plausible in such a system. In addition, the same model was also used to examine condensation diagrams which described how the dye molecule parameters and system temperature affected destruction of thermalization in the microcavity [18]. Due to the similarities between the thermalization processes in an optical microcavity and a plasmonic nanoparticle array, the results from both experimental and theoretical work in the field of photon condensates provide encouragement to finding a similar crossover from lasing to condensation in a plasmonic system.

Chapter 4

Experimental methods

This chapter describes the experimental tools required to create and investigate the plasmonic systems discussed in the previous chapters. First, the fabrication process and the geometrical design of the metallic nanoparticle arrays is presented. Second, the text describes the measurement procedure required to validate the optical properties of the fabricated structures and to observe both plasmonic lasing and BEC using optical equipment. Third, the optical setup used in the experiments and its possible effects on the results are presented in detail.

4.1 Sample fabrication

Nanoparticle arrays introduced in section 2.2 are fabricated on a $75.6 \pm 0.1 \times 25.0 \pm 0.1 \times 1.0 \pm 0.5$ mm^3 borosilicate glass substrate (Schott NEXTERION® Glass D). Figure 4.1 shows the different fabrication stages. The process begins by spin-coating 350 µl of polymethyl methacrylate (PMMA A4, 4% molecular weight), which is a positive resist, on a glass substrate. The substrate is spun for 90 seconds at 3000 RPM and then prebaked on a hot plate for 120 seconds at 175 °C in order to solidify the PMMA.

The desired patterns are drawn on the resist layer using electron beam lithography (EBL). The chemical structure of the positive resist is altered at the exposed areas which makes them soluble in the developer solvent. In order to prepare the sample for EBL, a 10 nm layer of aluminum is evaporated on the substrate (Figure 4.1(a)). It prevents electric charge from accumulating on the sample and also provides a reflective surface for the height sensor in EBL. The following parameters were used in the lithography process: 1500 µC dose, 5 nm resolution and step size, 5 nA beam current, 300 nm beam aperture and 100 kV acceleration voltage.

After the desired patterns have been drawn, the aluminum is etched away in AZ 351 B acid for 90 s. The pattern is developed by immersing the substrate in a 1:3 MIBK:IPA (methyl isobutyl ketone : isopropanol) solvent mixture for 20 s. The areas exposed to the electron beam in EBL dissolve and leave a mold of the desired structure on the substrate (Figure 4.1(b)). A 2 nm adhesive layer of titanium and a 50 nm gold layer is evaporated on the developed resist layer (Figure 4.1(c)). These metal layers form the nanoparticles after the unexposed resist and excess aluminum are removed. The rest of the resist layer is dissolved away in an overnight acetone lift-off (Figure 4.1(d)).

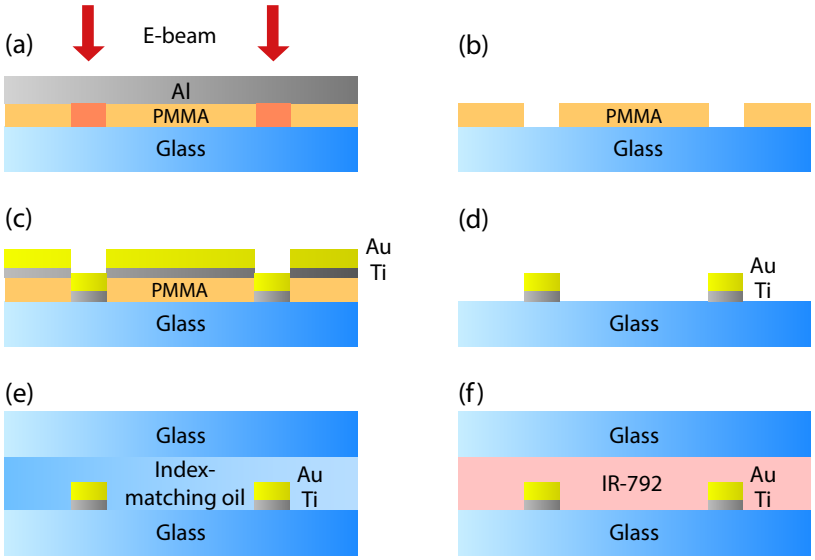

Figure 4.1: Sample fabrication stages. (a) Electron beam lithography. (b) Developed pattern on PMMA-layer. (c) Evaporation of metal layers. (d) Removal of PMMA-layer in lift-off. (e) Sample preparation for transmission measurements. (f) Sample preparation for lasing and BEC experiments.

The nanoparticle arrays are designed to have a clear band gap below the Γ-point. All arrays have a length of $d_y = 300$ μm and a width of $d_x = 100$ μm. The rectangular design allows one to investigate the propagation of SLR excitations along the lattice. The fabricated nanoparticles have a rectangular shape and they form a square array with periodicity $p = p_y = p_x$. The width of the particles is 100 nm and the length is 65 % of the array periodicity. An example of a finished nanoparticle array is shown in Figure 4.2. Multiple arrays are fabricated on the same substrate with p ranging from 580 nm to 620 nm. The transition between BEC to lasing is expected to occur as the periodicity is varied from 600 nm to 615 nm [10].

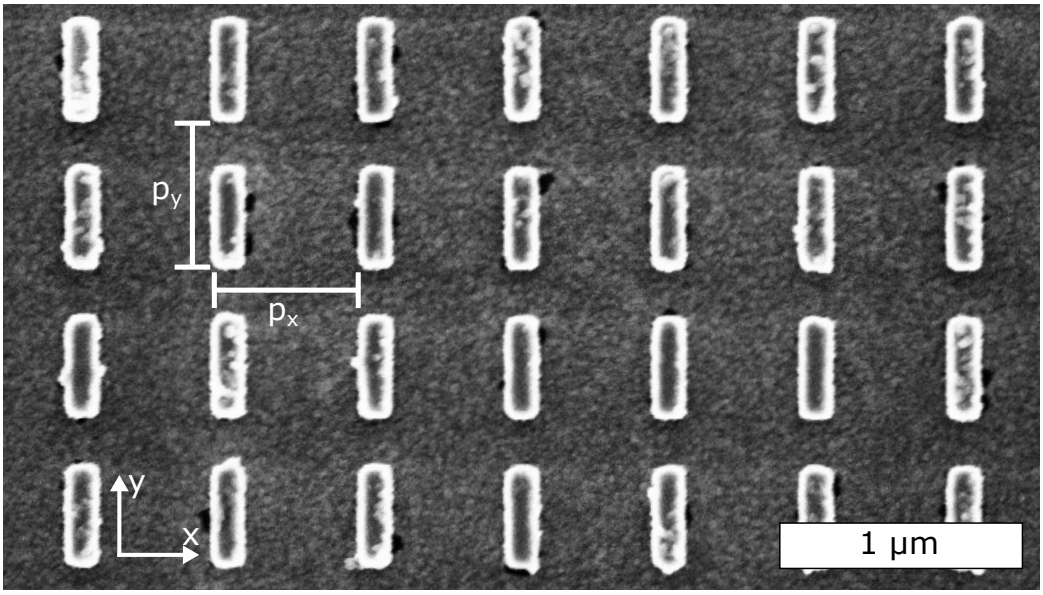

Figure 4.2: A scanning electron microscope image of a fabricated nanoparticle array with $p = 600$ nm. The length scale of the image is shown in the bottom right corner. The white arrows depict the coordinate system used in the text.

4.2 White light transmission measurements

In order to characterize the nanoparticle arrays their dispersions are examined using transmission measurements. The arrays are prepared for the experiment by covering the nanoparticles with index-matching oil whose refractive index corresponds to that of the glass substrate ($n = 1.52$). The oil layer is covered with another glass slide which effectively seals the nanoparticles inside an index-matching environment, see Figure 4.1(e).

The transmission of the samples is measured by focusing white light on the array and imaging the spectrum of transmitted light with a spectrometer. The measured spectrum then shows the dispersion of the SLR mode as a decrease in intensity as light is both absorbed and scattered as it passes through the array.

The focused beam of white light ensures that photons arrive to the array from multiple angles which correspond to different in-plane momenta in the array. Light coming from the sample is gathered with an objective whose back focal plane is focused via lenses to a vertical slit in front of the spectrometer. All light rays with identical in-plane momentum leave the sample at the same angle and meet at a single point at the back focal plane. The vertical slit filters incoming light whose horizontal momentum k_x is non-zero. Light at

each point of the slit is then refracted with a grating inside the spectrometer and the resulting momentum and energy resolved spectrum is captured with a charge-coupled device (CCD) camera. The optical path and the lens system are described in detail in section 4.4.

4.3 BEC and lasing measurements

In the BEC and lasing experiments the arrays are covered with a fluorescent dye solution which works as a gain medium in the system, see Figure 4.1(f). The dye used in the experiments is IR-792 perchlorate which absorbs and emits light in the near-infrared region of light. Its emission and absorption maxima are around 1.47 eV and 1.57 eV, respectively [10]. The molecules are dissolved in a solution of 1:2 DMSO:BA (dimethyl sulfoxide : benzyl alcohol) whose refractive index is equal to that of the glass. However, the refractive index of a dye solution may change depending on the dye concentration [39] and cause reflections at the glass-dye interface. A volume of 7 ± 0.11 µl of 50 mM solution is used to cover the arrays. Applying a larger volume will cause the molecule mixture to exude from the edges of the cover glass. The area of the cover glass is 575 ± 13 mm^2. The thickness of the molecule layer can be approximated by dividing the dye volume with the cover glass surface area. This gives an approximate thickness of 12 ± 0.6 µm.

In order to study the effect of the dye layer thickness, some of the measurements are performed using a tilted cover glass which is shown in Figure 4.3. The distance from the cover glass to the substrate glass is fixed from one edge of the sample with a small piece of tape. By fabricating the nanoparticle arrays at different locations on the substrate glass, it is possible to examine the plasmonic BEC and lasing processes with different molecule layer thicknesses. The tape used to separate the substrate and cover glass is Scotch®Magic™810 whose reported thickness is 0.06 mm [40]. The thickness of the molecule layer at different locations on the substrate is approximated by assuming that the layer thickness at the edge of the cover glass without tape is equal to the thickness of a regular sample: 12 ± 0.6 µm. The thickness l_{mol} in micrometers can then be calculated as

$$l_{mol} = 0.02h_y + 12 \pm (0.0002h_y + 0.6), \tag{4.1}$$

where h_y is the distance from the cover glass edge to the nanoparticle array in micrometers.

As described in section 3.2, the laser pump spot must be close to the edge of the array in order to see the dynamics of the thermalization process. The effect of the pump scheme on the BEC and lasing processes is investigated

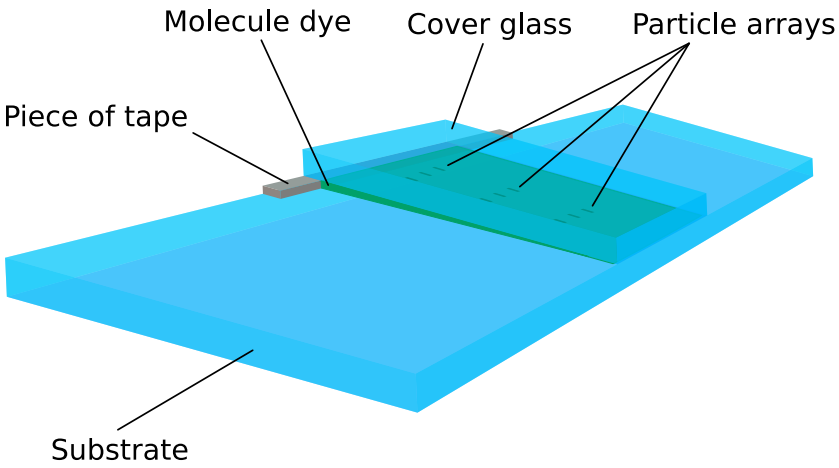

Figure 4.3: Prepared sample with a tilted cover glass to vary the molecule layer thickness over the nanoparticle arrays.

systematically by varying the spot location in y-direction. One measurement set is performed with the spot outside the array and three sets with the spot extending approximately 30 µm, 50 µm and 110 µm over the array.

The results of the BEC and lasing measurements are captured in a similar fashion as in the transmission experiments. The emitted light from the array is collected with an objective and focused via lenses to the spectrometer slit. Momentum and energy resolved spectra can be used to investigate how the SLR population propagates along one of the dispersion branches but it is also informative to look at how the thermalization occurs along the array. In this case, an additional lens is used to focus and magnify the real space image of the array to the center of the vertical spectrometer slit. Each point along the slit then corresponds to a y-coordinate on the array.

4.4 Experimental setup

The experimental setup used in the BEC and lasing experiments is presented in Figure 4.4(a). An ultrafast Astrella Ti:sapphire Amplifier is used to produce a laser beam at 1 kHz repetition rate at a wavelength of 800 nm. The beam can then be guided into an optical parametric amplifier (OPA) which is used to tune the pulse wavelength down to 750 nm in order to bring it away from the emission range of IR-792. The experiment can also be carried out using the 800 nm beam by bypassing the OPA, although in this case any pump reflections from the sample must be eliminated from the spectrum with a long pass filter.

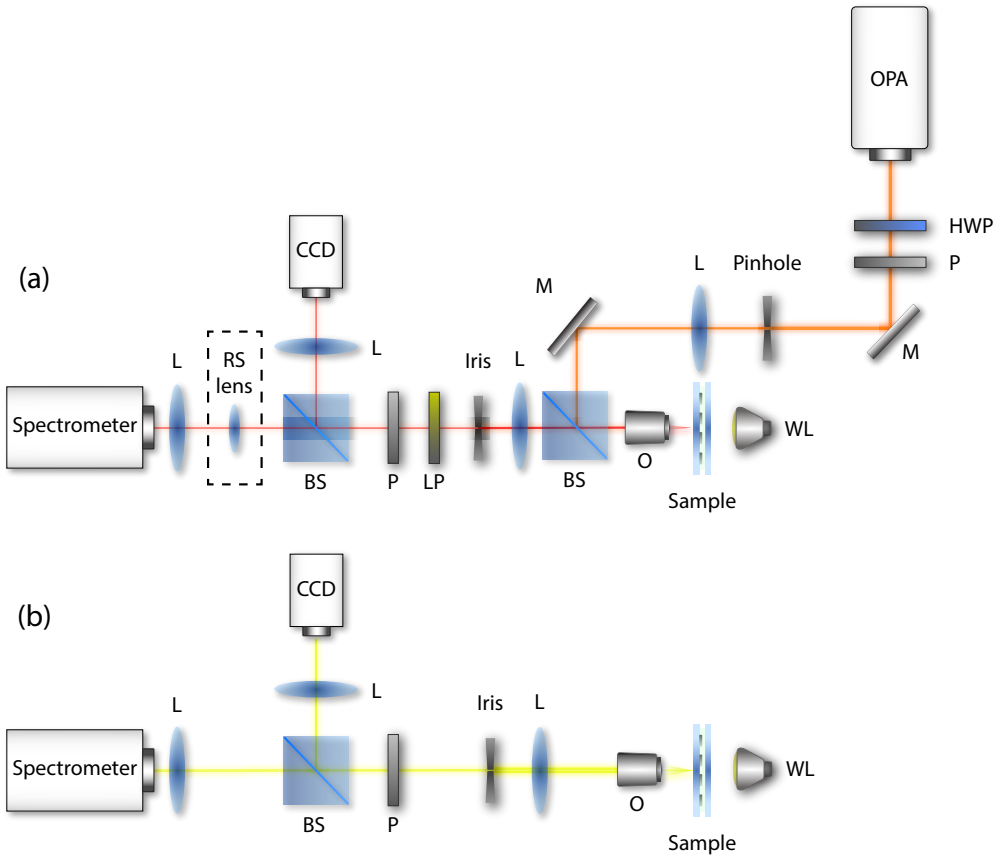

Figure 4.4: Schematics of the experimental configurations. (a) Configuration of the energy and y-position resolved measurements. The same setup is also used to measure angle and energy resolved data by removing the real space lens (RS lens). (b) Configuration of the transmission measurements.

Originally the pump beam is horizontally polarized, and first it is guided through power-adjusting optics. This includes a motor-controlled half-wave plate (HWP) and a horizontally oriented linear polarizer (P). The half-wave plate shifts the polarization direction of the linearly polarized light so that the angle θ between the orientation of the linear polarizer and the plane of polarization in the laser beam can be adjusted. The intensity of the laser beam then follows Malus's law which states that light intensity I after a polarizer is

$$I = I_0 \cos^2(\theta), \tag{4.2}$$

where I_0 is the intensity of the original beam [41]. This setup makes it swift to tune the beam power by adjusting the orientation of the half-wave plate.

Before entering the sample, the spot size of the laser beam is adjusted with an iris. A lens (L) with 200 mm focal length, a beamsplitter (BS) and a 10x infinity corrected objective (O) are used to draw an image of the iris to the sample so that the beam arrives perpendicularly to the nanoparticle arrays. The sample is placed on a sample holder so that the longer side of the nanoparticles (y-direction) is vertically oriented and the shorter side (x-direction) is horizontally oriented. Light emitted from the sample is captured with the objective and an infinity corrected tube lens (200 mm focal length). An 832 nm long pass filter (LP) removes possible pump laser reflections from the sample. A beamsplitter guides some of the light to a CCD camera which records an image of the sample. A white light halogen lamp (WL) can be used to illuminate the sample for the CCD camera. The rest of the light is guided through another lens (100 mm focal length) which focuses the back focal plane of the objective to the vertical slit in front of the spectrometer. Figure 4.4(a) also shows the additional RS lens used in the BEC experiments. Figure 4.4(b) shows the setup configuration for the transmission experiments. In this configuration, the long pass filter and RS lens are removed and the halogen lamp is the only source of light.

The optical paths of the setup configurations are shown in Figure 4.5 where the red and orange arrows represent an object and its image, respectively. Figure (a) shows the propagation of light rays in the angle-resolved measurement. The object is at a working distance f_{wd} from the objective which is depicted as a lens in the figure. Light rays propagating in the same direction meet at the back focal plane of the objective (x_1). The distance to the tube lens from x_1 is equal to the focal length f_{tube}. This results in an image of the object at the back focal plane of the tube lens (x_2). This is where the iris is located and where the CCD-camera is focused to. In order to image the back focal plane of the objective to the spectrometer, another lens (KS lens in the figure) is placed at focal length f_k from x_2. An image from x_1 is then focused to x_3 which is at the back focal plane of the last lens. This is where the spectrometer slit is located.

The objective used in the experiments is an infinity corrected Nikon Plain Fluor objective with 10x magnification and 0.3 numerical aperture. The tube lens is designed to work with the objective and together the magnification produced by the two components is equal to the magnification of the objective. In order to calculate the magnification of the entire setup, it is necessary to consider the lens and magnification equations. The lens equation relates the focal length f of a lens to the object distance d_o and image distance d_i such that

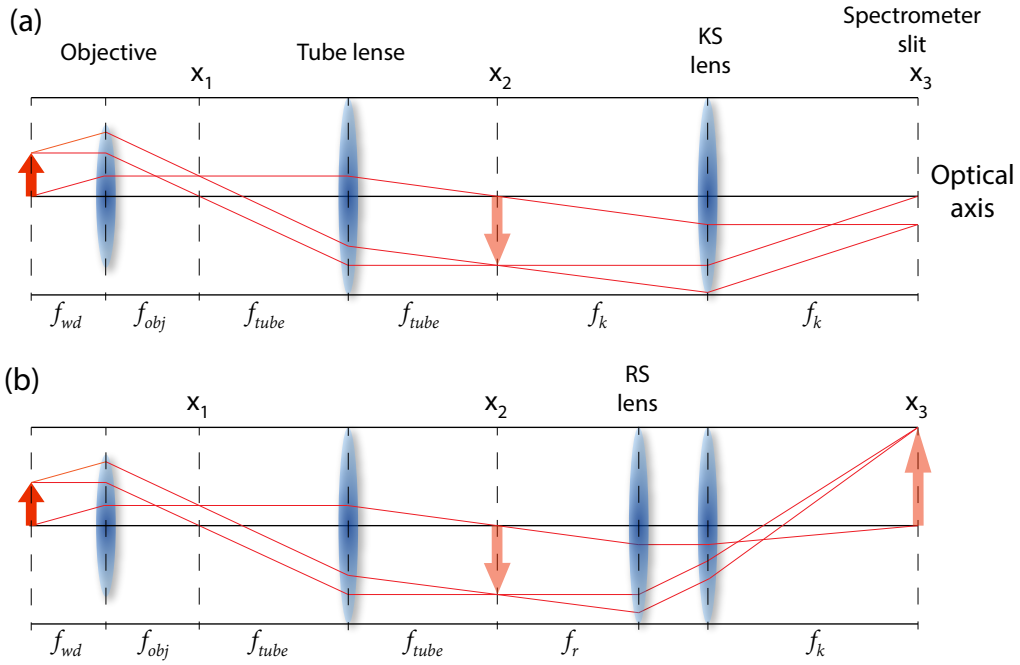

Figure 4.5: Illustration of light ray propagation in the experimental setup. (a) The optical path in the angle-resolved measurements. Light rays leaving the object (red arrow) at the same angle meet in the same point at the spectrometer slit (x_3). Additionally, a magnified image of the object (orange arrow) can be observed at the image plane x_2. (b) The optical path in the real space BEC measurements. An additional lens (RS lens) creates a magnified image of the object at the spectrometer slit without the need of adjusting other optical components.

$$\frac{1}{f} = \frac{1}{d_o} + \frac{1}{d_i}. \tag{4.3}$$

The magnification equation relates the magnification M of a single lens to d_o and d_i:

$$M = -\frac{d_i}{d_o}. \tag{4.4}$$

The negative sign in Equation (4.4) corresponds to an inverted image. First we consider a simple two-lens system. Two converging lenses are placed on an optical axis with distance d between them. The focal lengths of the lenses are equal to f_1 and f_2. An object is placed at the rear focal point of the first lens so that $d_{o1} = f_1$. Inserting this to Equation (4.3) shows that $d_{i1} \to \infty$

which means that the light rays from each point of the object are parallel. The image produced by the first lens is the object for the second lens such that $d_{o2} = d - d_{i1}$ The magnification of the two lenses M_{tot} is equal to the product of the individual magnifications M_1 and M_2:

$$M_{tot} = M_1 M_2.$$

Combining this with Equation (4.4) gives

$$M_{tot} = \frac{d_{i1}}{d_{o1}} \frac{d_{i2}}{d_{o2}} = \frac{d_{i1}}{d_{o1}} \frac{d_{i2}}{d - d_{i1}}.$$

Now set the limit $d_{i1} \to \infty$ to get

$$M_{tot} = \lim_{d_{i1} \to \infty} \frac{d_{i1}}{d - d_{i1}} \frac{d_{i2}}{d_{o1}} = \lim_{d_{i1} \to \infty} \frac{1}{d/d_{i1} - 1} \frac{d_{i2}}{d_{o1}} = -\frac{d_{i2}}{d_{o1}} = -\frac{f_2}{f_1}. \tag{4.5}$$

Equation (4.5) shows that the magnification of an object located at the rear focal point of the first lens is the ratio of the focal lengths.

Figure 4.5(b) shows the optical path with the RS lens in place. The focal length of the lens is smaller than the focal length of the KS lens ($f_r < f_k$) and it is placed so that its rear focal plane is at the image plane x_2. The magnification of the image at x_2 via the two last lenses is the ratio between their focal lengths according to Equation (4.5). Combining this with the magnification of the 10x objective and tube lens, the total magnification in the system with the RS lens becomes

$$M_{RS} = -10 \frac{f_k}{f_r}. \tag{4.6}$$

In the setup shown in Figure 4.5 the focal lengths of the tube lens, RS lens and KS lens are 200 mm, 60 mm and 100 mm, respectively. According to Equation (4.5), the magnification of the back focal plane of the objective in the angle-resolved measurements is $-\frac{1}{2}$. Inserting the focal lengths to Equation (4.6) gives a magnification of $16\frac{2}{3}$. As the size of the array is 300 μm, the height of the array image at the spectrometer slit is 5 mm. The height of the CCD array inside the spectrometer is 8 mm so it is comfortably able to image the entire array.

In addition to conducting the condensation and lasing measurements, a major part of this thesis was to construct the experimental setup described in this section. This included assembling and aligning the optical components shown in Figure 4.4 as well as calibrating the spectrometer to be used with an automated LabVIEW software. The most critical part of the construction

process was to align the angle-resolved light path shown in Figure 4.5 using a reference laser beam which defines the optical axis of the setup. In order to achieve good transmission efficiency and minimal optical aberration in the condensation and lasing measurements, the setup components were optimized for the near-infrared region of light.

4.5 Fabry–Pérot interference

Interference is the phenomenon of multiple coherent waves combining together to form a superposition of waves. The amplitude of the superposition is the sum of the component amplitudes. Constructive interference occurs when the waves are in the same phase and destructive interference when the waves are in opposite phases. This phenomenon can be observed with all types of waves which means that it is also present in the optical setup used in the BEC and lasing measurements.

The nanoparticle lattices used in the experiments are built on glass slides which function as a Fabry-Perot interferometer. A Fabry–Pérot interferometer can be constructed by placing two partly reflecting surfaces close to each other forming a transparent plate, see Figure 4.6. When light propagates through the plate, some of the light will reflect back from the interfaces. Reflections from the second surface continue to reflect and propagate back and forward inside the plate. Light will experience a phase shift due to the additional optical path which results in interference between the multiple reflections of light. This can be observed as alternating transmission maxima and minima on a wavelength spectrum. Maximum transmission occurs at frequencies ν_q for which

$$\nu_q = \frac{qc}{2nl\cos(\alpha)}, \quad q = 1, 2, ... \tag{4.7}$$

where l is the distance between the reflecting surfaces and α is the angle of the incident light inside the transparent plate [42]. The distance between adjacent transmission peaks in wavelength space, or the free spectral range, is

$$\Delta\lambda = \lambda_q - \lambda_{q+1} = c\big(\frac{1}{\nu_q} - \frac{1}{\nu_{q+1}}\big). \tag{4.8}$$

Inserting (4.7) into Equation (4.8) gives

$$\Delta\lambda = 2nl\cos(\alpha)\frac{1}{q^2+q}. \tag{4.9}$$

Substituting $q = 2nl\cos(\alpha)/\lambda_q$ gives

$$\Delta\lambda = \frac{\lambda_q^2}{2nl\cos(\alpha) + \lambda_q} \approx \frac{\lambda_q^2}{2nl\cos(\alpha)}. \tag{4.10}$$

Equation (4.10) can be used to match possible interference fringes in the spectra to the transparent layers in the sample and other optics.

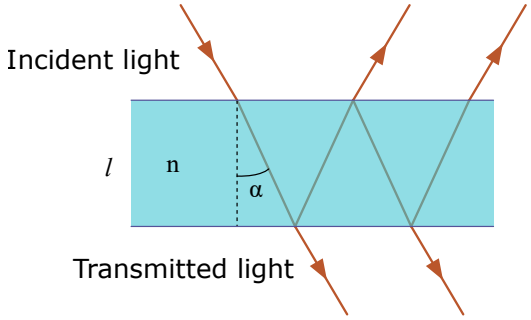

Figure 4.6: Fabry-Perot interference due to a thin glass slide. Multiple reflections in a transparent plate cause the transmitted light to interfere with itself.

Chapter 5

Results

This chapter presents the experimental results of the thesis. First, the transmission spectra of both the nanoparticle lattice and the fluorescent molecules are shown. Second, the text goes over the results from the BEC experiments which, in addition to reproducing the original plasmonic condensate, includes the effect of using a varying dye layer thickness and changing the pump geometry.

5.1 Transmission experiments

Examples of the measured white light transmission spectra are shown in Figure 5.1. The visible dispersions of the nanoparticle arrays demonstrate the features of the SLR modes in a metallic square array with rod-shaped nanoparticles. The (0,+1) and (0,-1) diffracted orders cross each other at the Γ-point and the modes propagating in different direction become coupled. The upper branch of the SLR mode shows the visible bright mode while the lower branch hosts the dark mode which is not detected in the transmission measurement. Transmission is lowest in the band edge of the upper SLR branch and the band gap between the lower and upper modes is also clearly visible.

Comparing Figures 5.1(a)-(d) it is evident that the band edge appears at a lower energy as the periodicity of the array is increased. This is in good agreement with Equation (2.6) which states that the energy of the Γ-point is inversely proportional to the array periodicity. As described in section 3.2, controlling the energy of the band edge is critical in the condensation process of SLR modes and in the BEC-lasing crossover. A distinctive SLR mode with high extinction and a clear band gap between the upper and lower

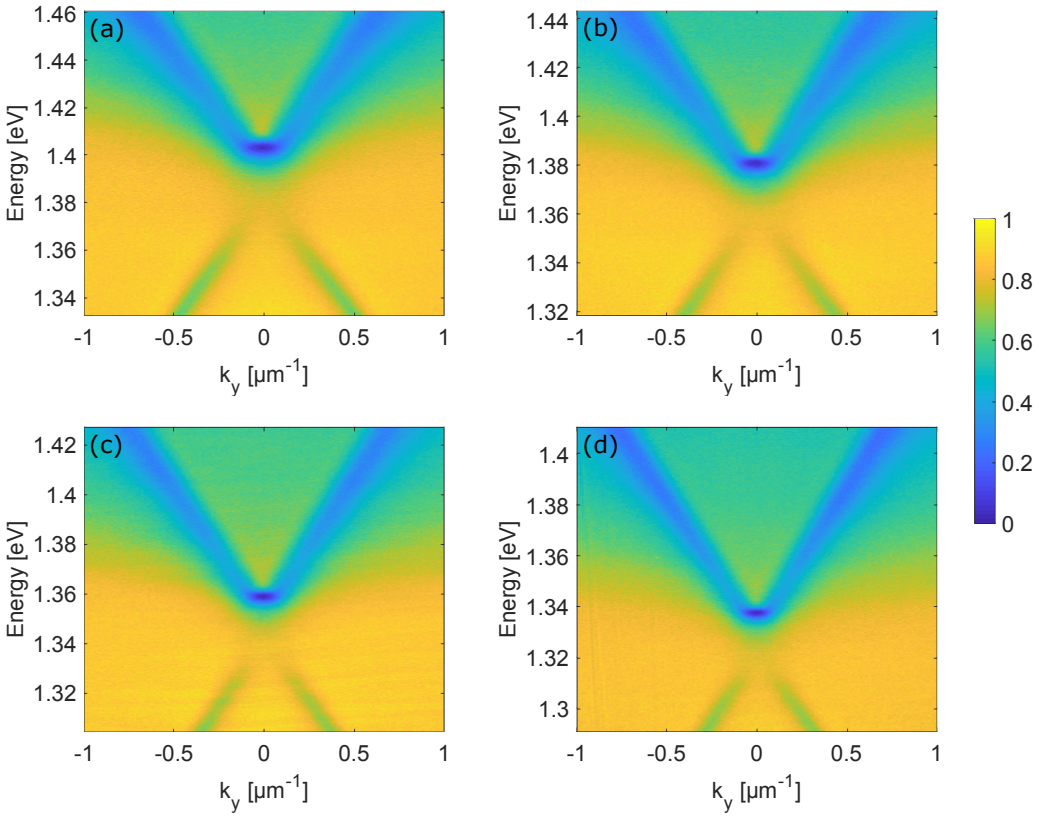

Figure 5.1: Angle-resolved white light transmission spectra of the nanoparticle arrays with periodicities (a) $p = 580$ nm, (b) $p = 590$ nm, (c) $p = 600$ nm and (d) $p = 610$ nm. The array dispersions show the coupled (0,+1) and (0,-1) diffracted orders with a band gap between the upper and lower branches.

bands assure that the quality of the samples is sufficient to move on to the BEC and lasing experiments.

In addition to the arrays, a transmission measurement was also performed using a thin layer of IR-792 in order to characterize its absorption properties. The results of this experiment are shown in Figure 5.2. The normalized absorption spectrum (blue line) shows a maximum at 1.53 eV and a small shoulder at 1.68 eV. The figure also shows the measured fluorescence spectrum of IR-792 under laser pumping (red line). The wavelength of the pump laser was 800 nm. An emission maximum can be observed at 1.46 eV. Emission above 1.473 eV is not shown as any possible reflections from the pump laser were filtered with an 832 nm long pass filter (black dashed line). The

absorption edge of IR-792 is located around 1.34 eV where the absorption goes practically to zero.

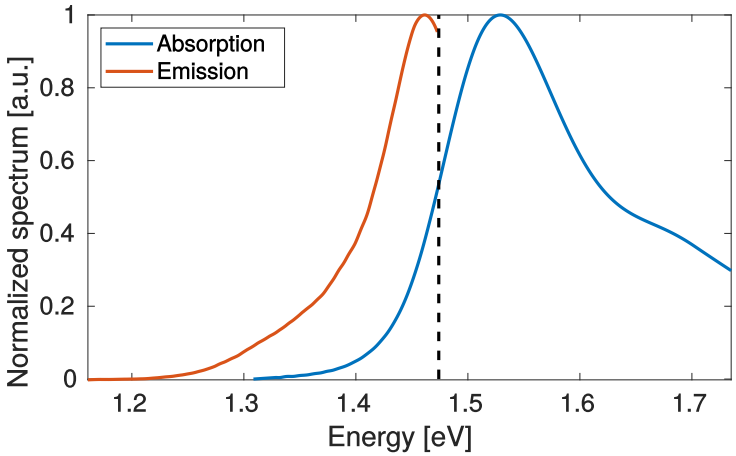

Figure 5.2: Normalized absorption (blue line) and emission (red line) spectra of IR-792 fluorescent dye. The long pass filter used in the emission measurement (LP832) is shown as a black dashed line.

5.2 Lasing and condensation experiments

5.2.1 Thermalization of SLR excitations and BE-distribution

Before moving on to the crossover between BEC and lasing, the functionality of the BEC system is demonstrated by producing a plasmonic condensate using a sample with $p = 600$ nm. The condensation of SLR excitations on such a sample has already been shown [10]. Figure 5.3 shows typical results from a successful plasmonic BEC measurement and their relation to the pumping geometry of the system. Figure (a) shows a normalized real space emission spectrum captured from the sample under laser pumping. The pumping scheme is presented on the left. The spectrum shows high-intensity emission from the pump around 1.42 eV at the beginning of the array. The photon part of the SLR population leaks out and we can examine the propagation of the SLR excitations by following the spectral evolution of the emission. As the population propagates along the array, the continuous cycles of absorption and re-emission in the molecule dye induce the thermalization process. This causes the emitted light to be red-shifted towards the band edge of the

array ($E = 1.34$ eV). As the excitations reach the band edge, the absorption edge of the molecules and the band gap of the array prevent the SLR population from jumping to the lower branch. A significant population of SLR excitations is formed at the lowest energy state which is shown as a sharp emission peak at 1.34 eV. The pump spot is cropped from the spectrum in order to bring out other features in the system.

Figure 5.3(b) demonstrates the same phenomenon by showing normalized emission spectra from the beginning and end of the array ($y = 50$ µm and $y = 260$ µm). At $y = 50$ µm a majority of the SLR population is still located close to the emission maximum of IR-792 due to laser pumping. Some of the excitations are already populating the band edge which causes a low intensity peak to appear at 1.34 eV. At $y = 260$ µm most of the SLR population propagating along the array has reached the band edge and a distinctive peak accompanied by a thermal tail has appeared. This distribution describes a macroscopic population of SLR excitations at the lowest energy state of the system, or a plasmonic Bose-Einstein condensate.

The evolution of the relative intensities is shown in Figure 5.3(c). The relative intensities are calculated by dividing the summed emission at (yellow line), above (green line) and below (red line) the band edge energy by the intensity from the entire spectrum. At the beginning of the array most of the emission is observed at energies above 1.34 eV while the relative intensities at and below 1.34 eV are close to zero. As the SLR population propagates along the array, the relative emission at the band edge increases and surpasses the emission from the high-energy states which demonstrates how the SLR excitations gradually accumulate to the band edge. Intensity below 1.34 eV stays relatively low throughout the array although increases in the end possibly due to small leakage from the lowest energy state. It must be noted that the measured total intensity decreases along the array due to losses in the metal particles which causes possible noise in the system to eventually bring the relative intensities close to each other.

In order to investigate the temperature related to the distribution of the thermalized tail in Figure 5.3(b), a Maxwell-Boltzmann curve was fitted to the measured data points at $y = 50$ µm. The plotted data points are mean intensity values over a 24 µm range. The fitting results are shown in Figure 5.4. Intensity in the figure is plotted in logarithmic scale which makes the MB-distribution to have a linear shape. The resulting MB-fit (red line) corresponds to a temperature of 301 ± 44 K with 95 % confidence bounds which is close to room temperature as expected [10]. The intensity peak at the ground state energy (1.34 eV) is excluded from the data points used in the fitting as the temperature of the distribution is determined by the thermalized tail.

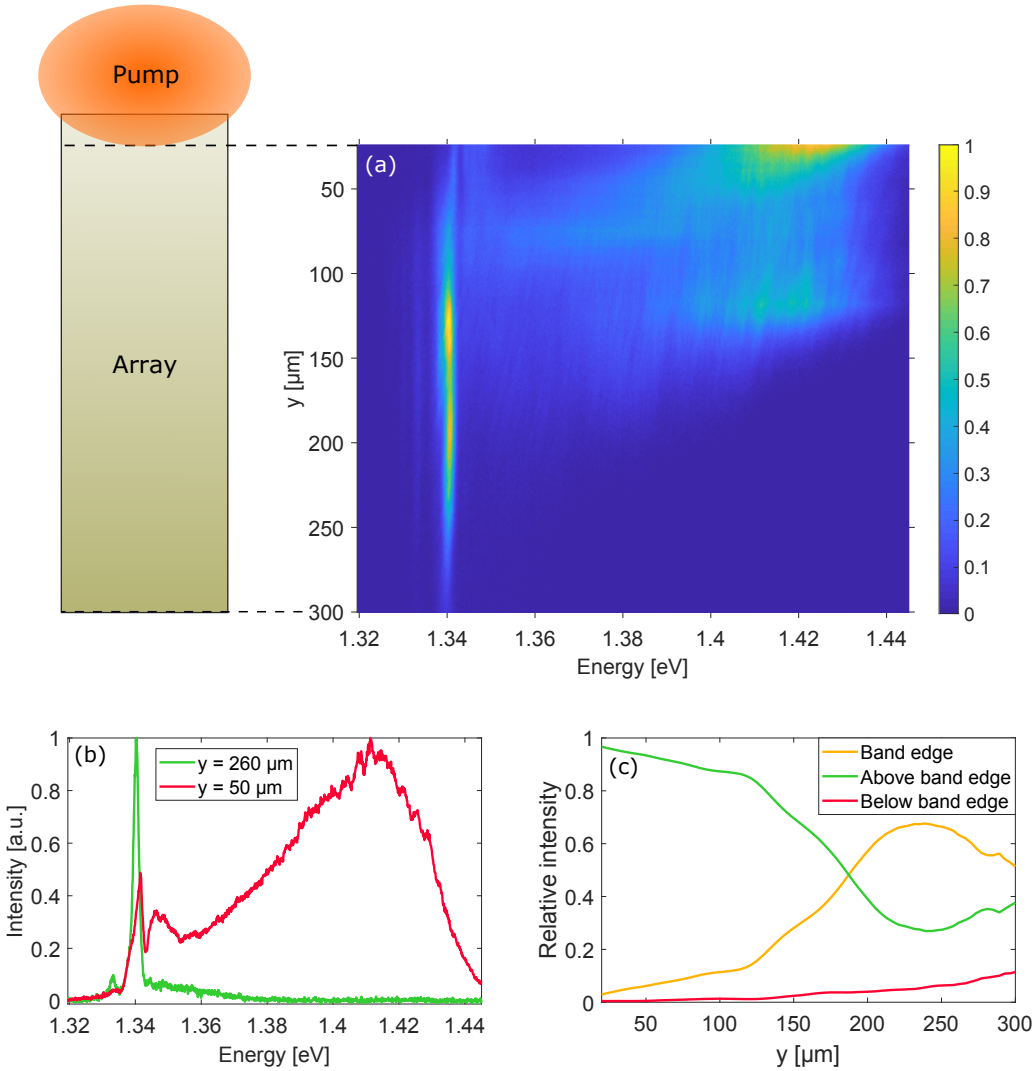

Figure 5.3: Plasmonic Bose-Einstein condensation experiment. (a) An exemplary real space energy spectrum attained from BEC measurements with 600 nm array periodicity. The y-coordinate corresponds to the distance from the beginning of the array as presented in the pump schematic on the left. The emission spectrum is normalized between maximum and minimum values and shows the thermalized SLR population accumulating to the band edge. (b) Normalized emission spectra obtained from different parts (y = 260 μm and y = 50 μm) of the spectrum in (a). The spectra are averaged over a 24 μm range. (c) Normalized relative intensities at, below and above the band edge energy (1.34 eV).

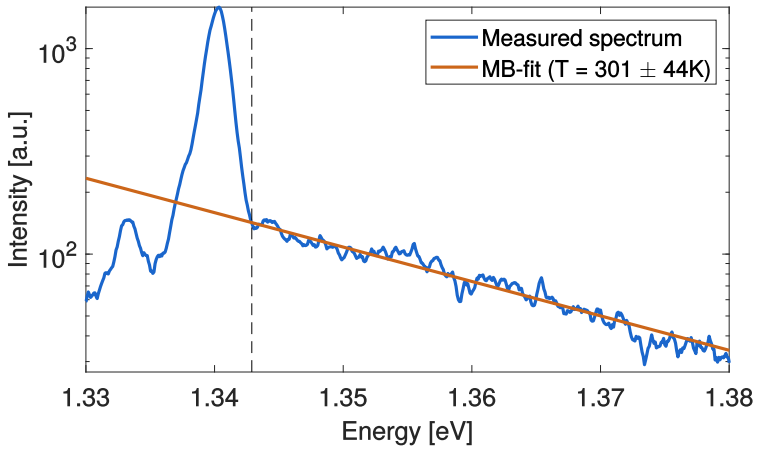

Figure 5.4: Maxwell-Boltzmann fit to experimental data from a BEC measurement. The blue line corresponds to a crosscut from the measured spectrum shown in Figure 5.3(a) at $y = 50$ µm. The spectrum is averaged over a 24 µm range. The red line shows a fitted Maxwell-Boltzmann fit with a temperature of 301 ± 44 K. Data points below 1.343 eV (black dashed line) are excluded from the fit. The periodicity of the nanoparticle lattice is 600 nm.

5.2.2 Varying molecule layer thickness

Figure 5.5(a) shows an emission spectrum of a lasing sample with period $p = 605$ nm under laser pumping. The spectrum shows a high-intensity lasing peak at 1.327 eV and the lower branch of the SLR mode around 1.313. However, a set of additional modes can be observed at energies above 1.33 eV which also appear in the BEC measurements frequently. The additional modes show alternating intensity minima and maxima in the k_y-direction. These modes seem like they could be caused by a Fabry-Pérot interference in the system.

A set of experiments was performed with a sample equipped with a tilted cover glass which allows one to measure identical samples with different dye layer thicknesses. The nanoparticle arrays on the substrate are located 2.8 mm, 5.6 mm and 8.4 mm from the substrate edge. Inserting these values into Equation (4.1) results in approximate molecule layer thicknesses of 18 ± 2 µm, 23 ± 3 µm and 29 ± 3 µm, respectively. The results from these measurements are shown in Figures 5.5(b)-(d) which show the crosscuts of angle and energy resolved experiments at $k_y = 0$. The lasing mode shows a low-intensity peak which could be caused by ineffective dye molecules fatigued after multiple measurements and the fact that the pump spot was located at the edge of

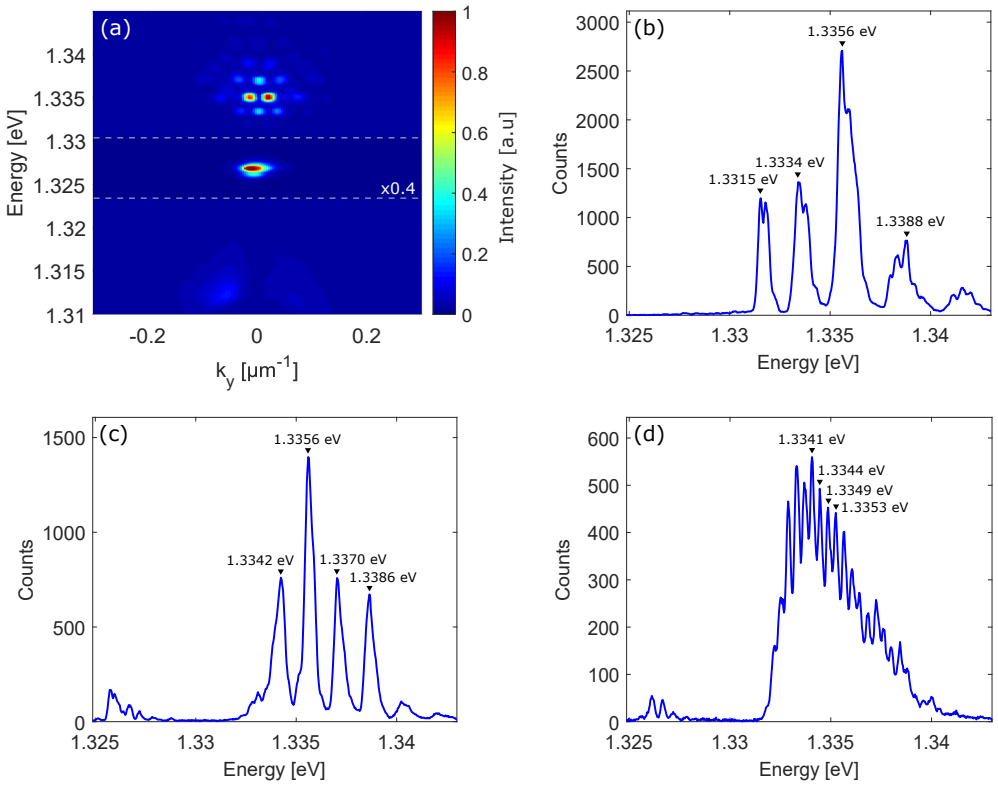

Figure 5.5: Peak anomalies in BEC and lasing spectra. (a) Normalized momentum and energy resolved spectrum of a nanoparticle sample ($p = 605$ nm) under laser pumping. The pump spot is positioned on top of the entire array which results in an intensive lasing peak at 1.327 eV. The intensity between 1.324 eV and 1.330 eV has been decreased by a factor of 0.4 to bring out the other features in the figure. (b)-(d) Crosscuts at $k_y = 0$ of the momentum and energy resolved spectrum from BEC measurements with different dye layer thicknesses. A sample with a tilted cover glass (see Figure 4.3) was used to set the molecule layer thickness to (b) 18 ± 2 μm, (c) 23 ± 3 μm and (d) 29 ± 3 μm.

the array. Figure (b) shows the measured spectrum with the thinnest dye layer (18 ± 2 μm) and it shows a sparse peak spacing with four definite peaks above 1.33 eV. Figure (c) shows the same measurement with a 23 ± 3 μm layer and it can be observed that the spacing of the peaks is now clearly denser. Figure (d) shows the spectrum with a dye layer thickness of 29 ± 3 μm and the peaks show an even denser spacing.

The locations of the peaks are shown in Table 5.1 in both electronvolts and nanometers. By calculating their free spectral range and inserting the values into Equation (4.10) one can calculate the thickness of a Fabry-Pérot interferometer which could cause the peaks. These values are also shown in the table. In the calculations the refractive index was set to 1.52. It is apparent that the thicknesses from the Fabry-Pérot calculations are an order of magnitude thicker compared to the approximations based on the sample structure. In addition, it seems that the peaks seen in Figure 5.5(d) are actually caused by interference in the glass substrates of the sample and therefore they are not caused by the same phenomenon which caused the peaks seen in (b) and (c). Similar interference was observed in all experiments when the spectrometer resolution was increased enough and the results from the Fabry-Pérot calculations are close to the substrate thickness (1 mm). Although the peak anomalies show a correlation with the molecule layer thickness, it seems that Fabry-Pérot interference in the dye layer does not directly explain them. It is also interesting that the intensity of the peaks gradually goes down with increasing dye layer thickness which suggests that a thin separation between the substrate and the cover glass is essential for the propagation of SLR excitations along the lattice. Indeed, repeating the BEC experiments with a thick dye layer (~ 0.8 mm) showed no propagation.

5.2.3 Pump geometry

So far in this work and in previous experiments [10] the location of the pump spot has been somewhat arbitrary as the convention has been to place it on the edge of the array without a precise reference point. One reason for this is the circular shape of the spot which mismatches the rectangular array shape. Improving this is critical for standardizing the experiment as the array should experience a uniform pump fluence for the most reliable results. This section presents the results from the BEC experiments where the location of the pump spot is placed in four different positions: one outside the array and three on top of it with increasing distance from the array edge.

Figure 5.6 shows results from a set of BEC-measurements where the pump spot is located outside the nanoparticle array. The pumping scheme is shown on the top left corner of the figure. In order to display the propagation of the SLR population throughout the array with a reasonable color scale, normalization was performed by dividing the spectrum at each y-coordinate by the maximum value found at that coordinate. This removes the visual effect of decreasing intensity and shows the thermalization process all the way to the end of the array. Figures (a)-(g) show the spectra measured with array periodicities 580 nm, 600 nm, 602 nm, 604 nm, 605 nm, 606 nm and 606.5 nm,

Table 5.1: Locations of the unknown intensity peaks from measurements with different molecule layer thicknesses and the corresponding thicknesses from Fabry-Pérot interference calculations. For each peak, the corresponding free spectral range is the wavelength separation to the adjacent peak with a shorter wavelength.

Approximated layer thickness [μm]	Peak locations [eV]	Peak locations [nm]	Calculated Fabri-Perot interference thickness [μm]
18 ± 2	1.3315	931.16	128.54
	1.3334	929.83	185.69
	1.3356	928.30	213.64
	1.3388	926.08	
23 ± 3	1.3342	929.28	256.28
	1.3356	928.30	291.62
	1.3370	927.33	290.40
	1.3386	926.22	
29 ± 3	1.3341	929.347	1021.1
	1.3344	929.14	815.99
	1.3349	928.79	1358.1
	1.3353	928.51	

respectively. With small periodicity ($p = 580$ nm) the SLR population shows the expected thermalization to the ground state followed by a jump across the band gap at 1.37 eV. Intensity decreases as the propagation continues in the lower SLR branch until the absorption edge stops the thermalization process. Figure (b) ($p = 600$ nm) shows the regular condensation case where the SLR population accumulates to the band edge (see Figure 5.3). Figures (c)-(e) show how the dynamics of the thermalization are affected by the increasing array periodicity. As the location of the SLR band edge is lowered in energy, the accumulation of the SLR excitations to the band edge occurs further down the array. In these figures it is also possible to see the appearance of the peak anomalies described in the previous section.

A major shift in the dynamics of the system can be observed in figures (f) and (g). With array periodicity $p = 606$ nm, some accumulation to the band edge can be observed but the spectrum does not display a distinctive mode which the SLR excitations would populate. In figure (g) ($p = 606.5$ nm) the band edge energy is below the absorption edge. The thermalization process via continuous cycles of absorption and re-emission is no longer able to reach the lowest energy state and the SLR population no longer accumulates to

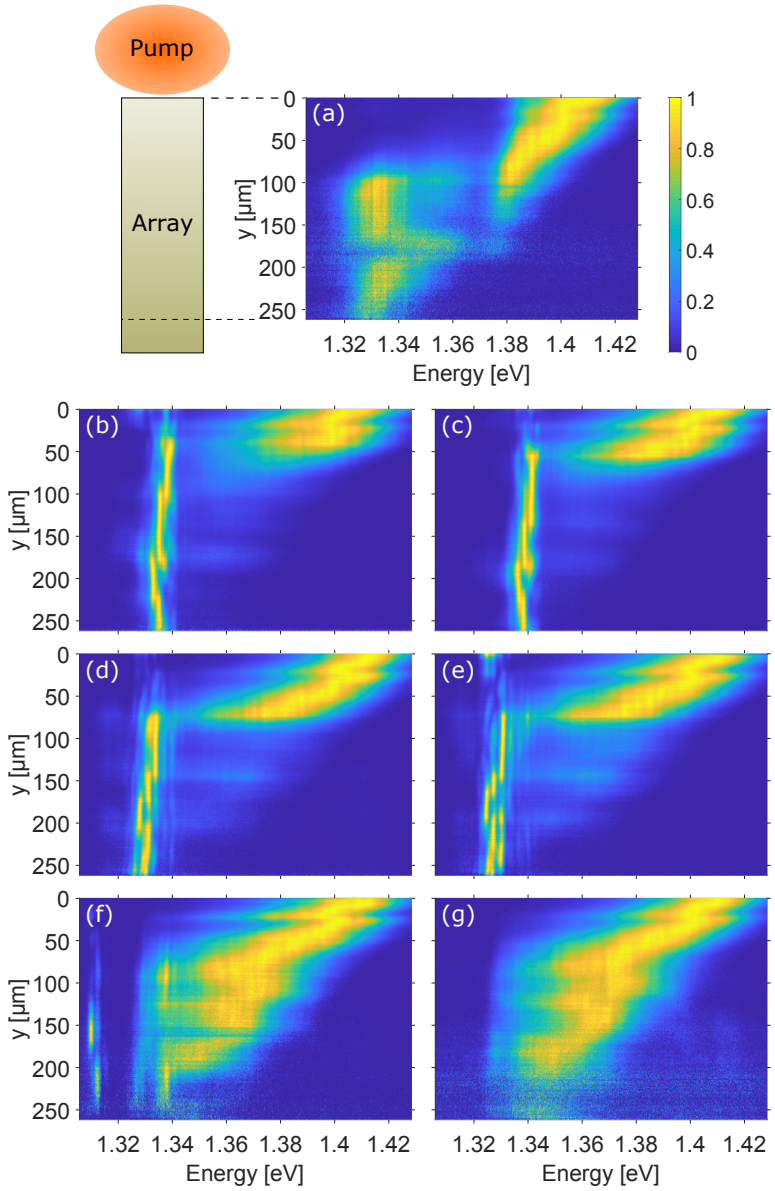

Figure 5.6: Propagation and condensation of SLR excitations under off-sample pumping. (a) Normalized real-space emission spectrum from BEC experiments with array periodicity $p = 580$ nm. The schematic on the left shows the pump location outside the array. (b)-(g) Emission from the same experiment as in (a) but with periodicities (b) 600 nm, (c) 602 nm, (d) 604 nm, (e) 605 nm, (f) 606 nm and (g) 606.5 nm. All spectra have been normalized such that the entire spectrum at each y-coordinate has been divided by the maximum intensity value found at that y-coordinate.

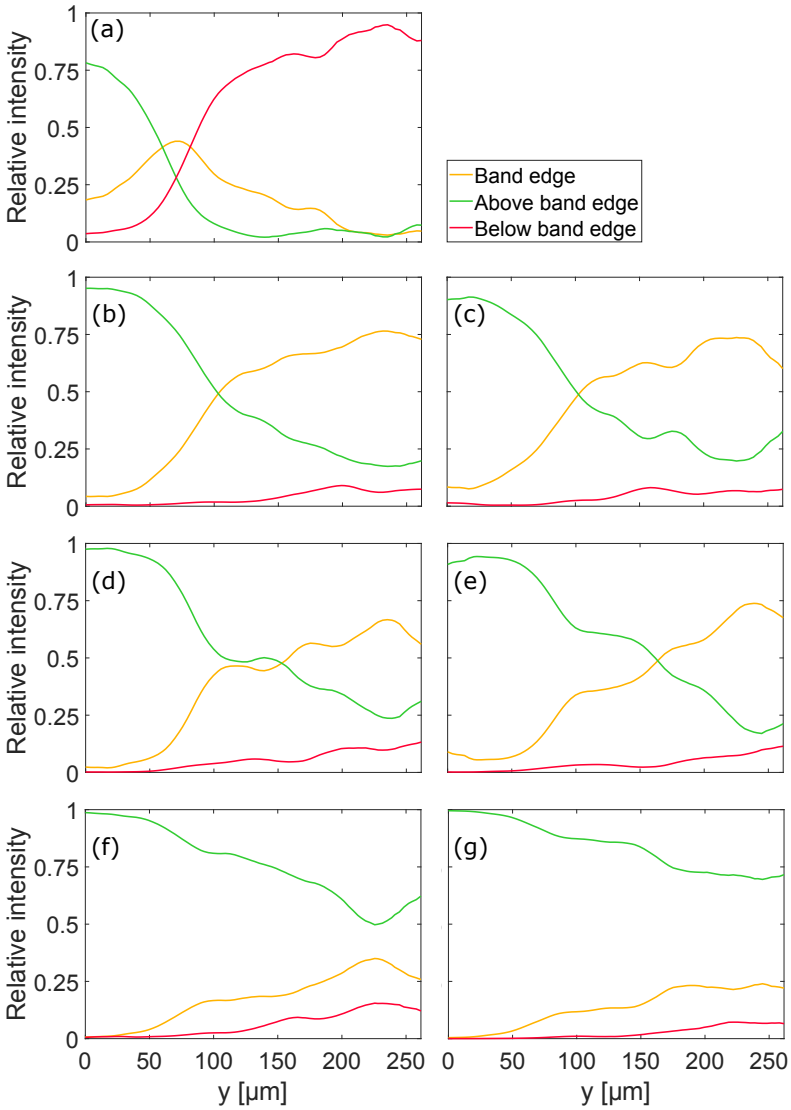

Figure 5.7: Relative emission intensities at (yellow line), above (green line) and below (red line) band edge energy calculated from spectra shown in Figure 5.6. The pump spot is located outside the array. (a)-(g) Calculated relative intensity values with array periodicities 580 nm, 600 nm, 602 nm, 604 nm, 605 nm, 606 nm and 605.5 nm, respectively.

the band edge. This is also the case with array periodicities above 606.5 nm. Surprisingly, it is possible to achieve this shift in the system dynamics with such a small change in the array periodicity. It must be noted that the exact periodicity where the accumulation ceased varied between 604 nm and 608 nm between experiment sets possibly due to bleaching experienced by the dye molecules.

Figures 5.7(a)-(g) show the relative intensities calculated from the spectra shown in Figure 5.6. Figure (a) (p = 580 nm) shows how the majority of the emission shifts first to the band edge from the high energy states and then likewise to the lower SLR branch. In figures (b)-(e) ($p = 600 - 604$ nm) the population at the band edge exceeds the population above it at a higher y-coordinate with increasing periodicity. In (f) (p =606 nm) and (g) (p = 606.5 nm) most of the emission remains in the high energy states throughout the array.

The results from the BEC experiments where the pump spot is placed on top of the array are shown in Figures 5.8-5.13. Figure 5.8 shows the emission spectra with the spot extending 30 μm over the array. Compared to the experiments with the pump spot outside the array (see Figure 5.6) the spectra show very little change. With p = 580 nm the emission still shows the thermalization along y and the jump across the band gap. Periodicities $p = 600, 602, 604$ and 605 nm display the condensation of SLR excitations and $p = 606$ nm and above only shows the thermalization as the absorption edge does not reach the band edge. Even the relative intensity diagrams (see Figure 5.9) show similar behavior compared to the case with the pump spot outside the array.

A significant change in the system dynamics can be observed when the spot is moved further on top of the array. Figure 5.10 presents the emission spectra from BEC experiments with the spot extending 50 μm past the array edge. Even with p = 580 nm the intensity below the band edge is significantly lower compared to the previous cases as a smaller portion of the SLR population jumps across the band gap. This is also evident from the relative intensity graph in Figure 5.11(a) where intensity below band edge never reaches 70 % whereas with the spot outside the array, it is up to 90 % close to the array end. With higher periodicities the story is similar. Although some population is still visible in the high energy range, all cases show a significant increase in intensity at the band edge, especially with p = 606 nm where the band edge now clearly shows an accumulation of excitations. The relative intensity curves in Figure 5.11 show that with periodicities p = 600-605 nm the band edge intensity remains clearly above 50 % excluding the beginning of the array. Only in the high periodicity case (p = 606 nm) the relative intensities at and above the band edge are both close to 50 %.

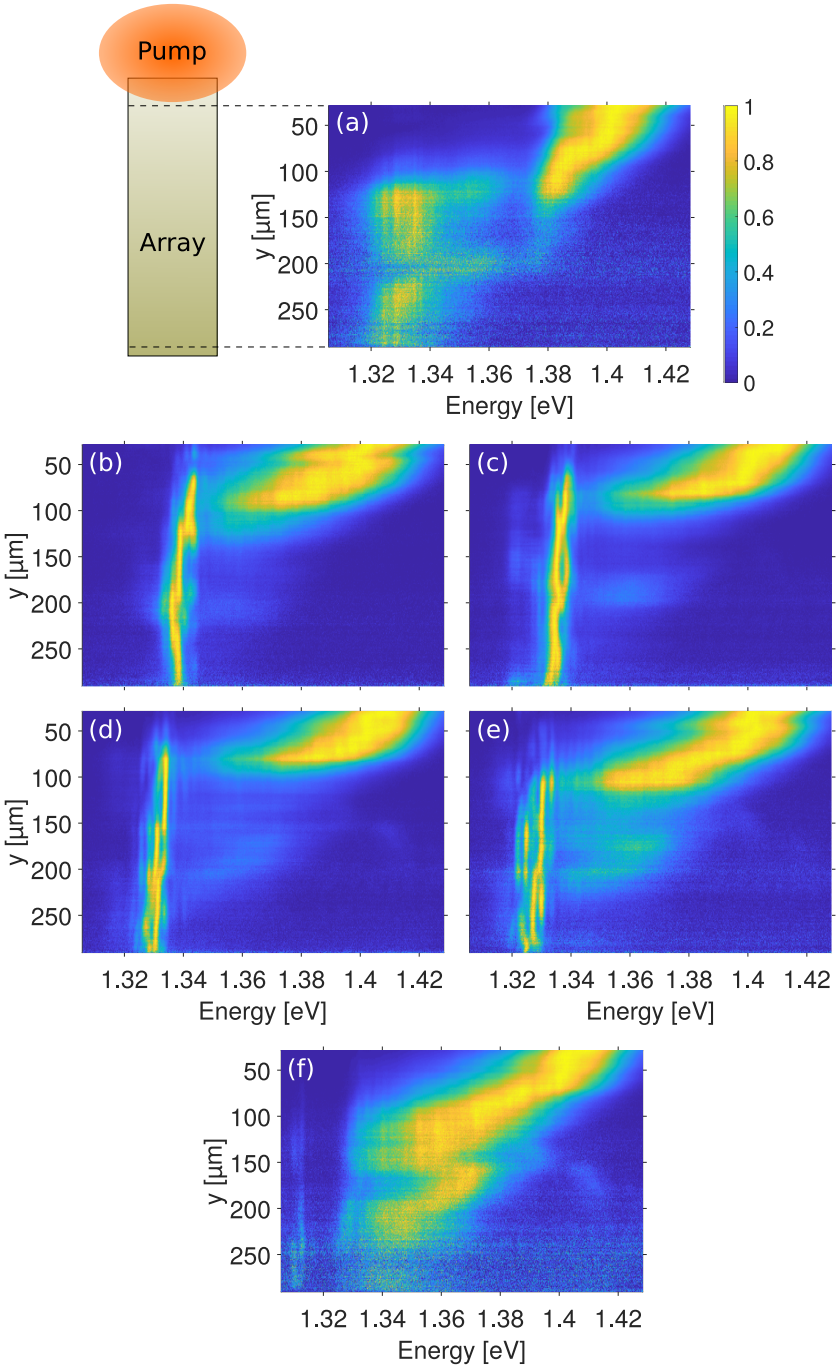

Figure 5.8: Normalized real-space emission spectra from BEC measurements with array periodicities (a) 580 nm, (b) 600 nm, (c) 602 nm, (d) 604 nm, (e) 605 nm and (f) 606 nm. The pump spot extends 30 µm over the array.

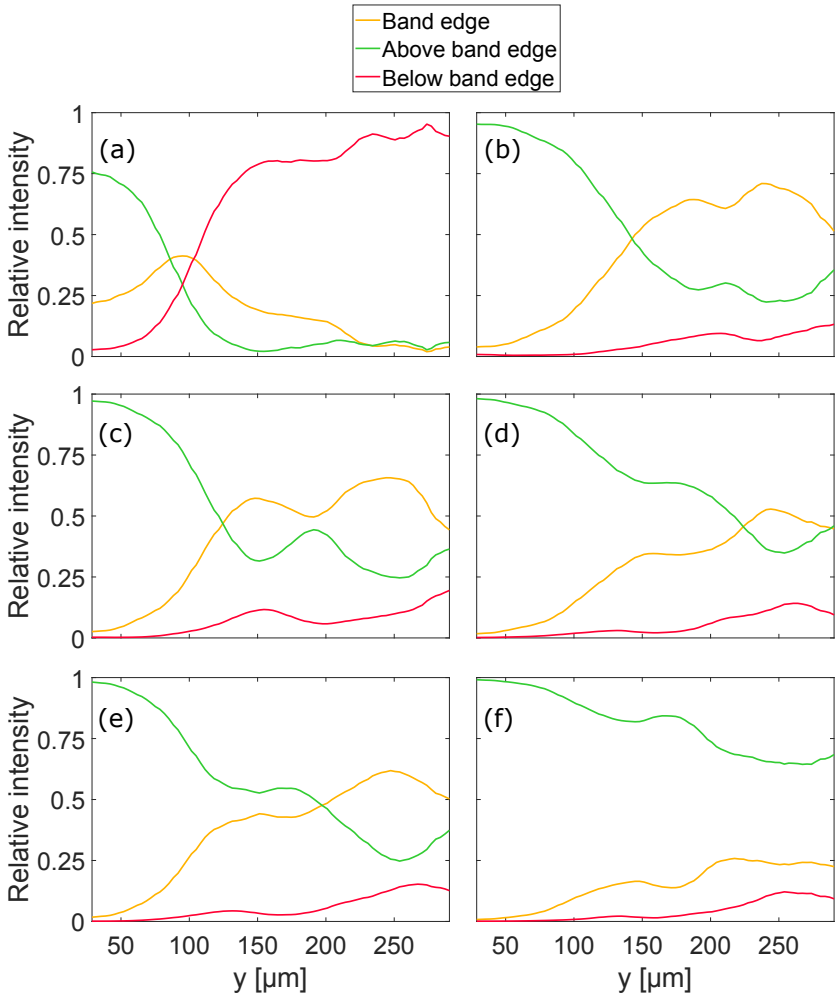

Figure 5.9: Relative emission intensities at (yellow line), above (green line) and below (red line) band edge energy calculated from spectra shown in Figure 5.8. The periodicities are (a) 580 nm, (b) 600 nm, (c) 602 nm, (d) 604 nm, (e) 605 nm and (f) 606 nm. The pump spot extends 30 μm over the array.

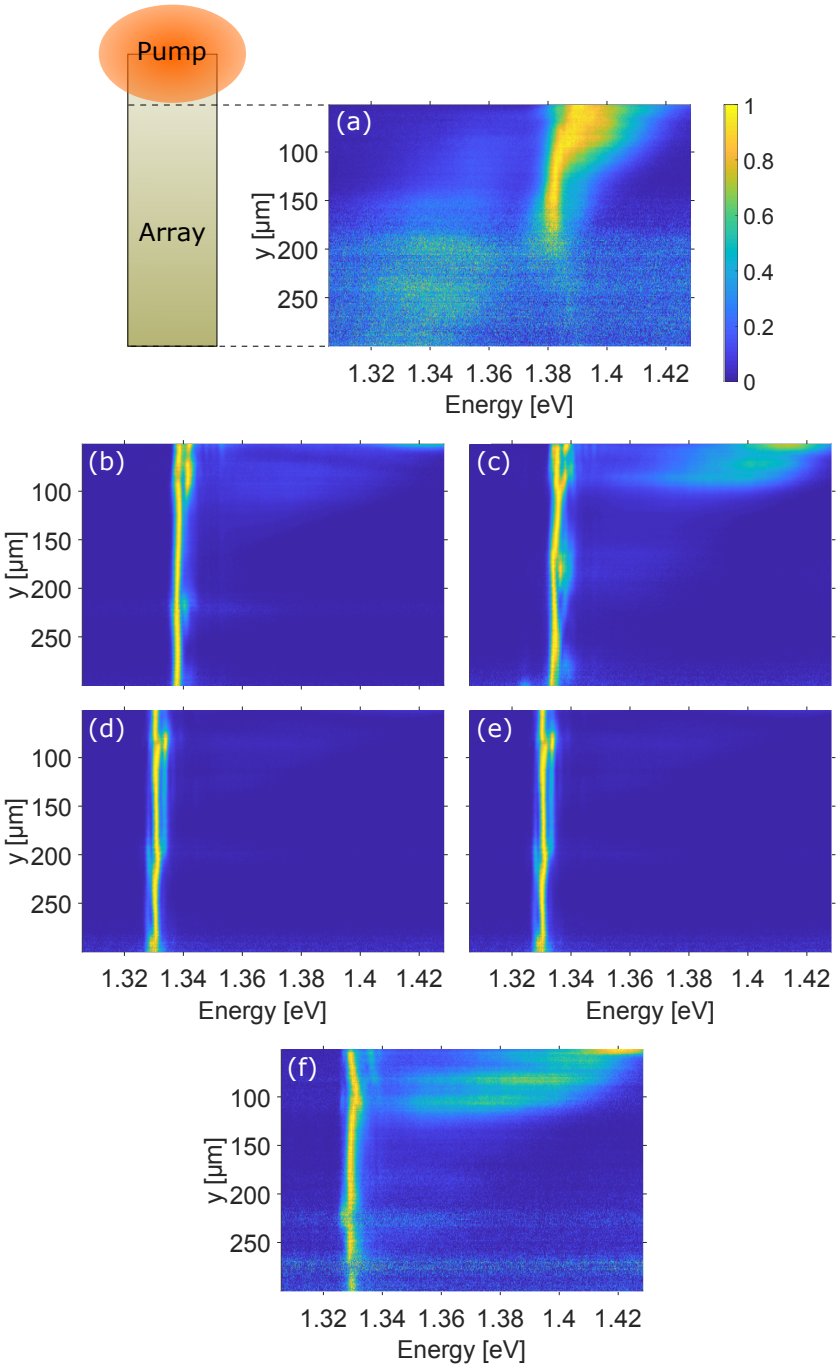

Figure 5.10: Normalized real-space emission spectra from BEC measurements with array periodicities (a) 580 nm, (b) 600 nm, (c) 602 nm, (d) 604 nm, (e) 605 nm and (f) 606 nm. The pump spot extends 50 μm over the array.

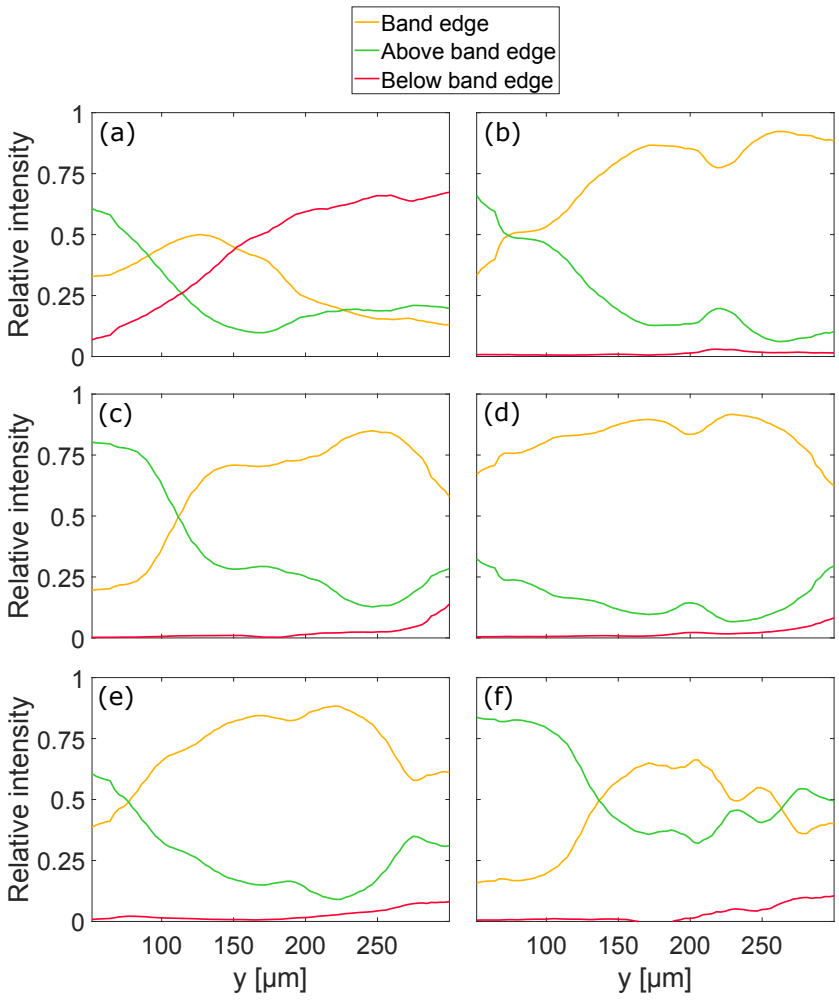

Figure 5.11: Relative emission intensities at (yellow line), above (green line) and below (red line) band edge energy calculated from spectra shown in Figure 5.10. The periodicities are (a) 580 nm, (b) 600 nm, (c) 602 nm, (d) 604 nm, (e) 605 nm and (f) 606 nm. The pump spot extends 50 μm over the array.

In the final case the spot is brought clearly on top of the array such that it extends 110 μm over the edge. The real space spectra in Figure 5.12 display how all periodicities seem to have transitioned towards the lasing case so that there is little to no intensity above or below the band edge. Looking at the relative intensities (Figure 5.13) reveals that although the band edge intensity is the dominant in all cases, there is still a significant amount of intensity in the high energy range. With $p = 580$ nm there is still some accumulation to the band edge towards the end of the array where the unfortunately high noise level eventually makes each relative intensity value almost equal. With increasing periodicity, the thermalization plays a smaller role in accumulating the intensity to the band edge as the lasing case becomes more apparent. This is particularly clear in the highest periodicity case ($p = 606$ nm) where more than 90% of the intensity is emitted from the band edge throughout the array. Interestingly, in almost all cases at $y \approx 150$ μm there is a small peak in the relative intensity above the band edge which could be due to the pump spot being out of focus. In this case the pinhole in the pump path will cause a diffraction pattern on the sample so that low-intensity diffraction fringes can excite dye molecules outside the actual pump spot.

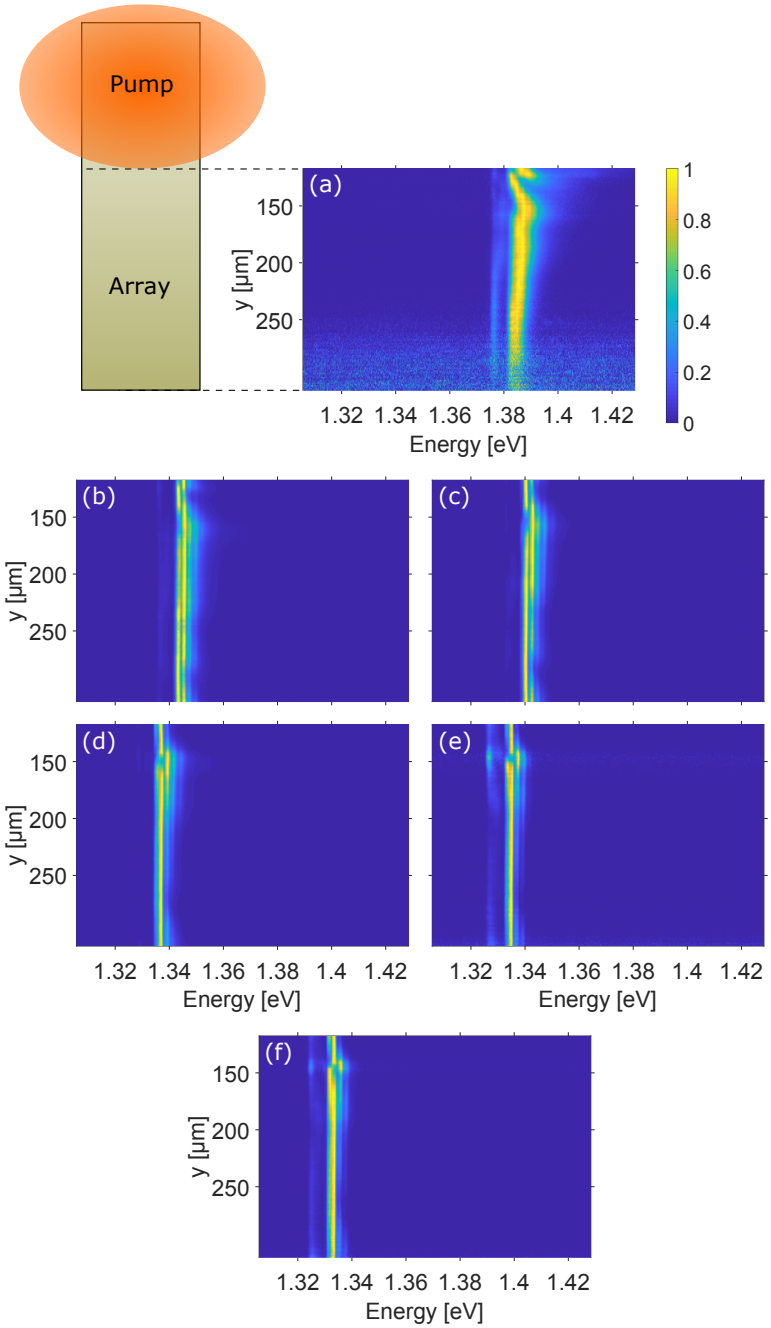

Figure 5.12: Normalized real-space emission spectra from BEC measurements with array periodicities (a) 580 nm, (b) 600 nm, (c) 602 nm, (d) 604 nm, (e) 605 nm and (f) 606 nm. The pump spot extends 110 µm over the array.

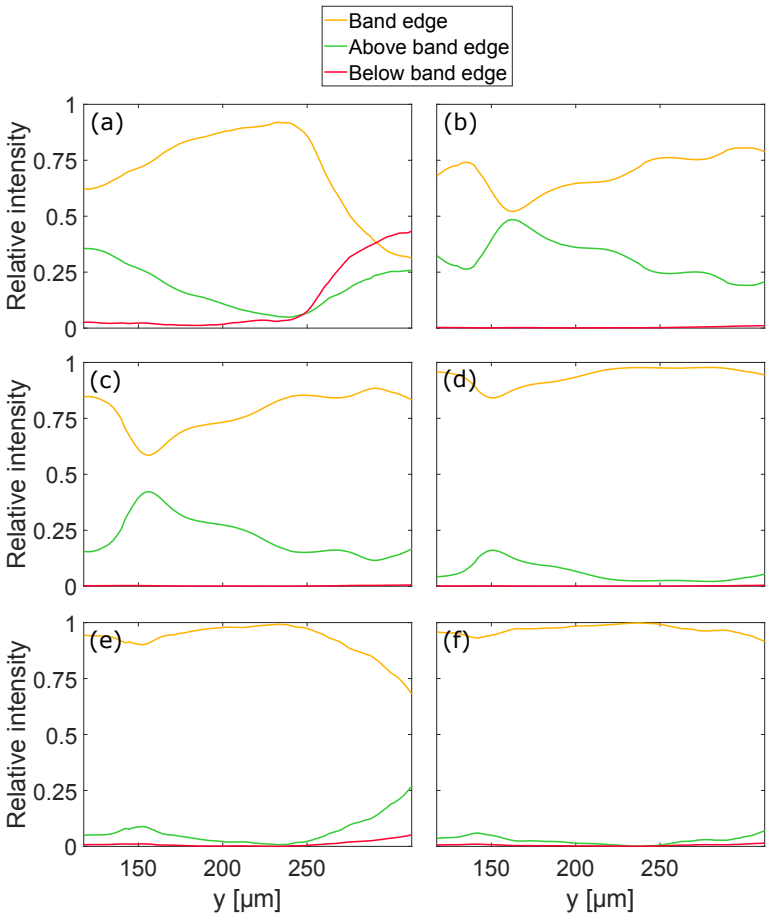

Figure 5.13: Relative emission intensities at (yellow line), above (green line) and below (red line) band edge energy calculated from spectra shown in Figure 5.12. The periodicities are (a) 580 nm, (b) 600 nm, (c) 602 nm, (d) 604 nm, (e) 605 nm and (f) 606 nm. The pump spot extends 110 μm over the array.

Chapter 6

Conclusions

The work done in the field of plasmonics has seen a surge of improvement in recent years regarding fundamental physical phenomena. Theory and experiments concerning coherent light production have lead to the realization of plasmonic Bose-Einstein condensation. Starting from the textbook condensates constructed with cold atomic gases, there has been a trend of moving towards room-temperature systems that utilize the interplay of thermalization and particle loss rates to produce non-equilibrium condensates. Similar dynamics govern the plasmonic system which, in some ways, has seen advances by following the steps of closely-related phenomena, such as the photon condensate. The strength of the light-matter interaction and the thermalization processes in these two systems are surprisingly similar and the recent work concerning a photonic lasing-condensation crossover have lead to promising expectations of a similar crossover in the plasmonic system.

Before advancing to investigate the effects of dye layer thickness and pump geometry, the original plasmonic condensate was reproduced and the shape of the thermal tail was in desirable agreement with the room temperature distribution observed in earlier work. Although there is no doubt the plasmonic system described in this thesis supports the condensation of SLR excitations, there are still some questions regarding the unidentified modes observed and whether they provide the necessary help for the SLR population to propagate along the nanoparticle array. The work shown here demonstrated a clear relation between the free spectral range of the peak anomalies and the dye layer thickness of the sample. Although a simple Fabry–Pérot effect did not seem to explain such behavior, the modes did seem to be connected to the dimensions of the sample instead of the nanoparticle array itself. With a thick dye layer, the peaks could no longer be observed within the limits of the measurement system but such modifications also prevented the SLR excitations from propagating properly. Although eliminating the excess modes

might not be possible without losing the spatial dynamics of the system, it is still important to understand their origin as they disturb the intensity distribution near the Γ-point. Possible sources could be waveguide modes that allow propagation in the dye layer or even resonances between two spatially separated arrays.

Introducing different pump geometries in the system had a major impact on the dynamics of the SLR population in the array. Placing the pump spot outside or close to the edge of the lattice had little to no effect on the samples with small periodicities where the SLR population reached the band edge and either accumulated there or jumped across the dispersion band gap. The absorption edge of IR-792 was either at the energy of the band edge or below it. However, at large periodicities, the thermalization process was suppressed before the SLR population could reach the band edge and there is no observable condensation let alone lasing. The required change in the lattice periodicity to see the SLR excitations no longer accumulate was surprisingly small: even a half a nanometer change impacted the system significantly. The periodicity where the SLR excitations stopped accumulating varied slightly, possibly due to dye molecule bleaching.

Shifting the pump spot towards the center of the array caused the system to transition towards the lasing case where most of the intensity is emitted from the band edge throughout the array. Even in samples with a small periodicity, only a small proportion of the total SLR population accumulated to the lowest state or jumped across the band gap via the thermalization process. With a large lattice periodicity, the shift to lasing behavior was even more distinct as more than 90% of the emission was measured from the band edge. This shows that in addition to the periodicity of the nanoparticle lattice, the location of the pump spot is critical in order to investigate the BEC-lasing crossover systematically.

Some of the most crucial future improvements to the experiments are related to the structure of the sample. Currently the only way to roughly control the thickness of the fluorescent dye layer is to vary the volume of the used dye or to use a tilted cover glass which was demonstrated in this thesis. However, both of these methods rely on the dye mixture to spread evenly across the substrate. A much better method would be to externally set the thickness by using an extremely thin mould between the glass interfaces. This would also prevent the solvent from evaporating from the edges of the cover glass which may cause the dye concentration to change over time.

Further challenges caused by the design of the system are related to the thin molecule layer which was estimated to be approximately 12 μm thick. Such a thin layer is quite vulnerable to bleaching as the dye molecules on top of the arrays are not continuously replaced with fresh molecules excluding

the area near the edge of the pump spot. As a result the same array cannot be measured consecutively multiple times without observing some variation in the results. The dye solution must therefore be replaced frequently and multiple measurement sets with identically prepared samples are difficult to accomplish.

Another challenge produced by the thin dye layer is that a high-powered pump beam is able to penetrate it and reflect from the cover glass back to the sample with a small delay. This may cause multiple SLR populations to begin the thermalization process in different parts of the array. It is therefore critical to control the pump beam incident direction for controlled results, in addition to the pump location. Applying a thicker molecule layer would be ideal for stable results as such samples would not require frequent dye solution replacing meaning multiple measurements could be performed with identical sample conditions. However, currently it seems that the only way to achieve proper propagation and thermalization of the SLR population in the array is to use a thin dye layer. It could be that the small dye volume keeps the emitted photons from dissipating into the solution without coupling to the SLR modes of the nanoparticle lattice.

As a final thought, the system described and investigated in this thesis has proven challenging yet extremely rewarding. The spatially propagating SLR excitations allow the thermalization process and its timescales to be examined with ease. The formation of the condensate and its distribution can be observed instantly and the processes behind it are easy to grasp. The system has some inconsistency problems which make measurements slightly difficult and there are still open questions related to the propagation of the SLR population. However, these imperfections can be improved by possibly revisiting the design and preparation routine of the samples. Among other non-equilibrium condensates, the plasmonic BEC demonstrates convincing and illustrative dynamics on an easily modifiable platform.

Bibliography

[1] R. K. Pathria. *Statistical Mechanics*. Elsevier, Burlington, 2nd edition, 1996.

[2] P. A. Lee, N. Nagaosa, and X.-G. Wen. Doping a Mott insulator: Physics of high temperature superconductivity. *Reviews of Modern Physics*, 78, Oct 2004. doi: 10.1103/RevModPhys.78.17.

[3] H. Deng, G. Weihs, C. Santori, J. Bloch, and Y. Yamamoto. Condensation of semiconductor microcavity exciton polaritons. *Science*, 298 (5591):199–202, 2002. ISSN 0036-8075. doi: 10.1126/science.1074464. URL `http://science.sciencemag.org/content/298/5591/199`.

[4] J. Kasprzak, M. Richard, S. Kundermann, A. Baas, P. Jeambrun, J. M. J. Keeling, F. M. Marchetti, M. H. Szymańska, R. André, J. L. Staehli, V. Savona, P. Littlewood, B. Deveaud, and L. S. Dang. Bose–Einstein condensation of exciton polaritons. *Nature*, 443:409–14, Oct 2006. doi: 10.1038/nature05131.

[5] S. O. Demokritov, V. E. Demidov, O. Dzyapko, G. A. Melkov, A. Serga, B. Hillebrands, and A. Slavin. Bose–Einstein condensation of quasi-equilibrium magnons at room temperature under pumping. *Nature*, 443: 430–433, Oct 2006. doi: 10.1038/nature05117.

[6] J. Klaers, J. Schmitt, F. Vewinger, and M. Weitz. Bose–Einstein condensation of photons in an optical microcavity. *Nature*, 468:545, Nov 2010. URL `http://dx.doi.org/10.1038/nature09567`.

[7] S. Zou, N. Janel, and G. C. Schatz. Silver nanoparticle array structures that produce remarkably narrow plasmon lineshapes. *The Journal of Chemical Physics*, 120(23):10871–10875, 2004. doi: 10.1063/1.1760740. URL `https://doi.org/10.1063/1.1760740`.

[8] V. G. Kravets, F. Schedin, and A. N. Grigorenko. Extremely narrow plasmon resonances based on diffraction coupling of localized plasmons

in arrays of metallic nanoparticles. *Physical Review Letters*, 101:087403, Aug 2008. doi: 10.1103/PhysRevLett.101.087403. URL `https://link.aps.org/doi/10.1103/PhysRevLett.101.087403`.

[9] T. Hümmer, F. J. Garcia-Vidal, L. Martín-Moreno, and D. Zueco. Weak and strong coupling regimes in plasmonic-QED. *Physical Review B*, 87, Mar 2013. doi: 10.1103/PhysRevB.87.115419.

[10] T. K. Hakala, A. J. Moilanen, A. I. Väkeväinen, R. Guo, J.-P. Martikainen, K. S. Daskalakis, H. T. Rekola, A. Julku, and P. Törmä. Bose–Einstein condensation in a plasmonic lattice. *Nature Physics*, 2018. ISSN 1745-2481. doi: 10.1038/s41567-018-0109-9. URL `https://doi.org/10.1038/s41567-018-0109-9`.

[11] T. K. Hakala, H. T. Rekola, A. I. Väkeväinen, J.-P. Martikainen, A. J. Moilanen, and P. Törmä. Lasing in dark and bright modes of a finite-sized plasmonic lattice. *Nature Communications*, 8, Jun 2016. doi: 10.1038/ncomms13687.

[12] J. Kasprzak, D. D. Solnyshkov, R. André, L. S. Dang, and G. Malpuech. Formation of an exciton polariton condensate: Thermodynamic versus kinetic regimes. *Physical review letters*, 101:146404, Oct 2008. doi: 10.1103/PhysRevLett.101.146404.

[13] J. Klaers and M. Weitz. Bose–Einstein condensation of photons and grand-canonical condensate fluctuations. In N. P. Proukakis, D. W. Snoke, and P. B. Littlewood, editors, *Universal Themes of Bose–Einstein Condensation*, chapter 19. Cambridge University Press, 2017.

[14] A. Chiocchetta, A. Gambassi, and I. Carusotto. Laser operation and Bose–Einstein condensation: Analogies and differences. In N. P. Proukakis, D. W. Snoke, and P. B. Littlewood, editors, *Universal Themes of Bose–Einstein Condensation*, chapter 20. Cambridge University Press, 2017.

[15] M. H. Szymańska, J. Keeling, and P. B. Littlewood. Nonequilibrium quantum condensation in an incoherently pumped dissipative system. *Physical Review Letters*, 96:230602, Jun 2006. doi: 10.1103/PhysRevLett.96.230602. URL `https://link.aps.org/doi/10.1103/PhysRevLett.96.230602`.

[16] J. Schmitt, T. Damm, D. Dung, F. Vewinger, J. Klaers, and M. Weitz. Thermalization kinetics of light: From laser dynamics to equilibrium

condensation of photons. *Physical Review A*, 92:011602, Jul 2015. doi: 10.1103/PhysRevA.92.011602. URL `https://link.aps.org/doi/10.1103/PhysRevA.92.011602`.

[17] P. Kirton and J. Keeling. Nonequilibrium model of photon condensation. *Physical Review Letters*, 111:100404, Sep 2013. doi: 10.1103/PhysRevLett.111.100404. URL `https://link.aps.org/doi/10.1103/PhysRevLett.111.100404`.

[18] P. Kirton and J. Keeling. Thermalization and breakdown of thermalization in photon condensates. *Physical Review A*, 91, Oct 2015. doi: 10.1103/PhysRevA.91.033826.

[19] P. Hofmann. *Solid State Physics: An Introduction*. John Wiley & Sons, 2nd edition, 2015.

[20] H. Raether. *Surface Plasmons on Smooth and Rough Surfaces and on Gratings*. Springer-Verlag, 1988.

[21] A. V. Zayats, I. I. Smolyaninov, and A. A. Maradudin. Nano-optics of surface plasmon polaritons. *Physics Reports*, 408:131–314, Mar 2005. doi: 10.1016/j.physrep.2004.11.001.

[22] L. Novotny and Hecht B. *Principles of Nano-optics*. Cambridge University Press, New York, 2006.

[23] A. V. Zayats and I. I. Smolyaninov. Near-field photonics: Surface plasmon polaritons and localized surface plasmons. *Journal of Optics A: Pure and Applied Optics*, 5(4):S16–S50, 2003. doi: 10.1088/1464-4258/5/4/353. URL `https://doi.org/10.1088%2F1464-4258%2F5%2F4%2F353`.

[24] E. Hutter and J. H. Fendler. Exploitation of localized surface plasmon resonance. *Advanced Materials*, 16:1685–1706, Oct 2004. doi: 10.1002/adma.200400271.

[25] R. J. Moerland, T. K. Hakala, J.-P. Martikainen, H. T. Rekola, A. I. Väkeväinen, and P. Törmä. Strong coupling between organic molecules and plasmonic nanostructures. In S. I. Bozhevolnyi, L. Martin-Moreno, and F. Garcia-Vidal, editors, *Quantum Plasmonics*, chapter 6. Springer, 2017.

[26] B. Auguié and W. L. Barnes. Collective resonances in gold nanoparticle arrays. *Physical Review Letters*, 101:143902, Sep 2008. doi: 10.1103/PhysRevLett.101.143902. URL `https://link.aps.org/doi/10.1103/PhysRevLett.101.143902`.

[27] W. L. Barnes, T. W. Preist, S. C. Kitson, and J. Sambles. Physical origin of photonic energy gaps in the propagation of surface plasmas on gratings. *Physical review B, Condensed matter*, 54:6227–6244, Oct 1996. doi: 10.1103/PhysRevB.54.6227.

[28] B. T. Draine and P. J. Flatau. Discrete-dipole approximation for scattering calculations. *Journal of the Optical Society of America A*, 11(4):1491–1499, Apr 1994. doi: 10.1364/JOSAA.11.001491. URL `http://josaa.osa.org/abstract.cfm?URI=josaa-11-4-1491`.

[29] P. W. Milonni and J. H. Eberly. *Laser Physics*. John Wiley & Sons, Hoboken, New Jersey, 2010.

[30] D. J. Griffiths. *Introduction to Quantum Mechanics*. Prentice Hall, Inc., Upper Saddle River, NJ 07458, 1995.

[31] S. J. Blundell and K. M. Blundell. *Concepts in Thermal Physics*. Oxford University Press Inc., New York, 2nd edition, 2010.

[32] M. H. Anderson, J. R. Ensher, M. R. Matthews, C. E. Wieman, and E. A. Cornell. Observation of Bose–Einstein condensation in a dilute atomic vapor. *Science*, 269(5221):198–201, 1995. ISSN 0036-8075. doi: 10.1126/science.269.5221.198. URL `http://science.sciencemag.org/content/269/5221/198`.

[33] K. B. Davis, M.-O. Mewes, M. R. Andrews, N. J. van Druten, D. S. Durfee, D. M. Kurn, and W. Ketterle. Bose–Einstein condensation in a gas of sodium atoms. *Physical Review Letters*, 75:3969–3973, Nov 1995. doi: 10.1103/PhysRevLett.75.3969. URL `https://link.aps.org/doi/10.1103/PhysRevLett.75.3969`.

[34] D. W. Snoke, N. P. Proukakis, T. Giamarchi, and P. B. Littlewood. Universality and Bose–Einstein condensation: Perspectives on recent work. In N. P. Proukakis, D. W. Snoke, and P. B. Littlewood, editors, *Universal Themes of Bose–Einstein Condensation*, chapter 1. Cambridge University Press, 2017.

[35] M. Planck. *The theory of heat radiation*. P. Blakiston's Son & Co, 1012 Walnut Street, Philadelphia, 1914.

[36] R. A. Nyman and B. T. Walker. Bose–Einstein condensation of photons from the thermodynamic limit to small photon numbers. *Journal of Modern Optics*, 65(5-6):754–766, 2018. doi: 10.1080/09500340.2017.1404655. URL `https://doi.org/10.1080/09500340.2017.1404655`.

[37] Y. B. Zeldovich and E. Levich. Bose condensation and shock waves in photon spectra. *Soviet Physics—JETP*, 28(6):1287–1290, Jun 1969.

[38] R. Chiao. Bogoliubov dispersion relation for a 'photon fluid': Is this a superfluid? *Optics Communications*, 179:157–166, Aug 1999. doi: 10.1016/S0030-4018(99)00615-X.

[39] W. Mahmood bin Mat Yunus. Refractive index of dye solution. *Applied Optics*, 28(20):4268–4269, Oct 1989. doi: 10.1364/AO.28.004268. URL `http://ao.osa.org/abstract.cfm?URI=ao-28-20-4268`.

[40] 3M Stationery & Office Supplies. Product information sheet scotch® magic™ tape 810, Oct 2008. URL `https://www.hillnmarkes.com/ASSETS/DOCUMENTS/ITEMS/EN/mmm810p10k_technicaldatasheet.pdf`.

[41] M. Mandfield and C. O'Sullivan. *Understanding Physics*. John Wiley & Sons in association with Praxis Publishing Ltd, Chichester, West Sussex, 1998.

[42] B. E. A. Saleh and M. C. Teich. *Fundamentals of Photonics*. John Wiley & Sons, Hoboken, New Jersey, 2nd edition, 2007.